**Media and Devices for Management of Airborne Contaminants**

A Thesis

SUMBITTED TO THE FACULTY OF THE

UNIVERSITY OF MINNESOTA

BY

Myles Devin Hicks

IN PARTIAL FULFILMENT OF THE REQUIRMENTS

FOR THE DEGREE OF

MASTER OF SCIENCE

David B. Kittelson, Advisor

January 2023

## Acknowledgements

The studies presented in this thesis were made possible by a gift presented from Cummins Filtration. I thank them for their generosity in funding the projects, as well as the technical expertise and advising from Daniel Potratz.

I thank my advisor, David Kittelson, for his support and guidance through the course of both projects. It was a pleasure to work with him and further myself in this area of research.

I would like to recognize my colleagues at the T.E. Murphy Engine Research Lab for moments of valuable deliberation and the cherished perspective each of them provided. I would also like to acknowledge the late Darrick Zarling for sharing his expertise in programming data acquisition and instrument control systems.

## Abstract

This thesis presents two projects pertaining to media and devices for the management of airborne contaminants. The projects were completed consecutively and have each been separated to their respective chapters.

*Investigation of the Temperature Dependent Effects in Crankcase Aerosol Control Devices*

Oil aerosols formed in the crankcase of reciprocating engines are a significant source of particulate matter and may lead to engine component degradation when used in closed crankcase ventilation (CV) systems or constitute a significant emission source in open CV systems. In modern CV systems, filtration or inertial separation is used to collect oil particles. These devices are highly efficient over a range of flow rates and temperatures; however, some system conditions result in a decrease in efficiency with increasing temperature in a manner not predicted by theory.

Experiments were performed on a bench system that introduced atomized oil particles into a clean, pre-heated, air stream that was conveyed isothermally through a heated duct to an oven containing the removal device, either a coalescing filter or an inertial separator, followed by another heated section and an exit duct. The aerosol was sampled using identical upstream and downstream isokinetic sampling systems and characterized using a Dekati Electrical Low-Pressure Impactor (ELPI) that measured particle concentration and size in the range from 0.043 to 8.46μm aerodynamic diameter.

Neither single fiber efficiency (SFE) filtration theory nor physical arguments describing the performance of the inertial separator predict a significant dependence of

total and fractional efficiency and most penetrating particle size (MPPS) on temperature in the range explored here, 25 to 115°C, but in many cases our measurements show MPPS shifting to smaller size and total efficiency decreasing with increasing temperature. These observations are consistent with the hypothesis that, at device temperature, the particles being processed are smaller than the particles being measured, at room temperature. Particles shrink by evaporation as they pass through the heated sections, but cool and grow by condensation as the sample cools in the sampling lines or in the exit duct.

Reported carbon number distributions of typical lubricating oils and evaporation kinetics indicate that droplets in the size range investigated may lose more than half of their mass under temperature conditions, up to 115°C, found in typical crankcase removal devices under engine high-load conditions. These droplets are in a dynamic balance with their vapors and may change during sampling and measurement. Great care must be taken in design of systems used to characterize devices intended to remove volatile droplets and interpretation of measurements made, as the size of the particles measured may not be the same as the size of particles passing through the device.

*Evaluation of Media and Low-Cost Gas Sensors for Indoor Air Quality Measurement*

The second project was motivated by increasing interest in high efficiency indoor air purification devices for control of airborne contaminants. Filtration is a commonly used method for removing particulate matter and improving air quality. An emerging field is the study of impregnated media, where the same highly efficient particle removal media can be engineered to also capture pollutant gases. We set out to evaluate the pollutant gas removal effectiveness for a set of carbon-impregnated media, where the pollutant gases under investigation were CO, $CO_2$, NO, $NO_2$, and $SO_2$. Another feature of the study was

that the sensors used were relatively low-cost sensors and a detailed evaluation of their performance was performed. Part of the motivation for using low-cost sensors was the possibility of using them for real-time performance of media in actual air purification devices.

The goal of the study was to evaluate 3 different carbon-impregnated media and a set of 6 low-cost gas sensors on a test bench designed to determine pollutant gas concentration as well as the removal efficiency. Tests were performed at ambient temperature conditions with relative humidity controlled from 5-60%, characteristic of indoor residential or commercial conditions. Five of the sensors used were Alphasense B4 series low-cost gas sensors, for monitoring CO, $SO_2$, NO, $NO_2$, and a combination $NO_2$ and ozone sensor. These were electrochemical type sensors. The sixth sensor was a non-dispersive infrared sensor for measuring $CO_2$.

The pollutant gas sensors were assessed for concentration accuracy, sensor noise, and response time. We found that sensor accuracy was acceptable under both humid and dry conditions for the NO, CO, and $CO_2$ sensors. Concentration accuracy was also acceptable for the $NO_2$ and $SO_2$ sensors, though indicated concentrations did not agree with expected values during media testing. This was due to concerns with the dilution air supply. Sensor noise observed was higher than specification for CO and $SO_2$, where $SO_2$ encountered the greatest deviations from manufacture specification. With respect to response times, it was found that the $CO_2$ and CO sensors were slower than manufacturer specification, the $NO_2$ and $NO_2/O_3$ matched specification, and the NO and $SO_2$ sensors were faster than specification.

The pollutant gas removal efficiency for each gas, media, and humidity combination was calculated and presented. The influence of humidity on removal effectiveness was observed, wherein humid conditions resulted in decreased pollutant gas removal efficiency. Removal efficiencies were very low for CO and $NO_2$. They were somewhat higher for NO, $SO_2$, and $CO_2$, most notably under dry conditions. This work demonstrated the efficacy of using LCGSs for media evaluation.

# Table of Contents

List of Tables

# List of Figures

# Chapter 1: Overview of the Two Studies

Liquid aerosols are produced from many natural and industrial actions wherein liquid particles are suspended in the air. Typical mists occurring naturally include fog, forest secretion, sea-water spray, and geyser steam. Industrial liquid aerosols are produced via thermal, mechanical, and chemical processes such as condensing, evaporating, spraying, splashing, injecting, shearing, and in chemical reactions. These liquid aerosols can be a valuable product or potentially harmful to society and the environment. In either account, harmful aerosols must be contained or treated in an efficient manner.

## *1.1 Investigation of the Temperature Dependent Effects in Crankcase Aerosol Control Devices*

The objective of this project was to determine the influence of temperature on the performance of systems designed to remove particles from crankcase fumes. Two types of CV (crankcase ventilation) particle removal devices were evaluated on an ISO 17356-4 test bench designed to determine device fractional particle removal efficiencies. Tests were performed under isothermal conditions to a maximum temperature of 115°C, characteristic of what might be expected with an engine operating under high-load conditions. Four different lubricating oils were tested with the main difference being volatility. Particle size distributions and concentrations were measured using a Dekati Electrical Low-Pressure Impactor.

Measurements were made upstream and downstream of the CV devices to determine the particle removal efficiency. The results showed an unexpected dependence of

efficiency on device temperature. It is hypothesized that as oil droplets pass through these devices, liquid and vapor are in dynamic equilibrium causing droplets to shrink when heated and grow when cooled. In this study upstream and downstream measurements were made at room temperature so that when the devices were heated, particles passing through the device were smaller than particles being measured.

## *1.2 Evaluation of Media and Low-Cost Gas Sensors for Indoor Air Quality Measurement*

A test bench utilizing mainly low-cost gas sensors (LCGS) was designed and built. It has been used to evaluate the performance of carbon impregnated filtration media, focusing on gas removal performance. The LCGS and media were being evaluated for potential incorporation into indoor air purification systems. Each of the low-cost gas sensors were Alphasense B4*x* type electrochemical sensors except one, which was a nondispersive infrared sensor (NDIR). The LCGS were evaluated for: (1) gas concentration accuracy, (2) sensor noise, and (3) response time. For each media tested, the influence of gas type, concentration and relative humidity on pollutant gas removal effectiveness was evaluated. Carbon dioxide was used as both a test gas, and as a tracer gas to monitor system dilution of pollutant span gases.

# Chapter 2: Investigation of the Temperature Dependent Effects in Crankcase Aerosol Control Devices

## *2.1 Introduction*

There is a small amount of leakage of combustion products past the piston rings of reciprocating engines, approximately 1% [1, 2]. This leakage can lead to an increase in crankcase pressure and damage to engine components if not managed [3, 4]. These crankcase fumes are composed of aerosolized lubricating oil and leakage gases from the combustion chamber. In practice, they are either recycled to the engine inlet or vented to the atmosphere. Unfortunately, if untreated, they may foul intake components, or if vented to the atmosphere can constitute a significant emission source[5, 6]. As a result, devices for removing crankcase fumes have been developed by numerous manufacturers. The two most common management techniques are positive crankcase ventilation (PCV) and open crankcase ventilation (OCV) [5]. In either method, efficient aerosol removal devices play a vital role. Specifically, in PCV systems, an efficient removal device will protect downstream engine components from degradation [3, 4, 7], and in OCV systems will minimize emissions vented to the atmosphere, which are considered part of the vehicle's exhaust emissions and are regulated by the EPA. Crankcase aerosol emissions may be minimized by a combination of reduced particle generation [8] and efficient particle removal devices [1, 9]. This study focused on the characterization and measurement of the performance of the latter.

The test facility used in this study is similar to that described in ISO 17536-2 "Road vehicles - Aerosol separator performance test for internal combustion engines - Part 2:

Laboratory test method", but with the added capability to operate the filtration test bench at greater elevated temperatures, simulating engine-like conditions, including typical high-load engine bay temperatures.

Positive crankcase ventilation appears most often in light-duty applications [5]. A PCV system usually operates wherein low pressure at the intake manifold of an internal combustion engine (ICE) draws the crankcase vapors to the intake duct, often first through an oil particle removal device, to be mixed with intake air for re-combustion [1], [5]. A well-documented issue with PCV systems, especially in turbocharged applications, is the fouling of components downstream [3, 4]. In turbocharged engine applications the oil aerosol is directed from the PCV system to the compressor side of the turbocharger. This has been shown to promote oil coking on compressor blades, leading to compressor degradation, gradual loss of boost pressure and increases in the potential for component failure [3].

Open crankcase ventilation (OCV) is the other common method for crankcase fume control, most often in medium and heavy-duty compression ignition (CI) applications [5]. In OCV, the crankcase particles are also reduced with an oil particle removal device, then exhausted to the atmosphere. When considering regulated vehicle emissions, crankcase fumes (gas and particles) must be included with vehicle tailpipe emissions, either physically or mathematically [7].

The EPA recently proposed a design standard requiring all heavy-duty highway CI engines from 2027 model year onward to be equipped with closed CV systems [7] likely promoting research and development on PCV systems.

In this study, two different types of crankcase particle removal devices: a coalescing filter and a rotating inertial device, both commonly used with medium and heavy-duty CI engine applications [1, 9–11] were tested using aerosols generated from lubricating oils with different physical properties over a variety of flow and temperature conditions. In ISO 17536-4 the highest temperature test condition specified is 80°C. In this study, the devices were tested under isothermal conditions up to 115°C because under typical high-load conditions, crankcase aerosol temperatures may be in the range of 80°C to 110°C. The size range of the particles used in these tests, by design, is in the same range as the oil droplets typically found in crankcase fumes. By both number and mass weightings, most of the particles are larger than the most penetrating particle size (MPPS) of the removal devices.

The test results described below show that the particle removal efficiency of these devices appears to depend on temperature in a manner not predicted by theory. It is hypothesized that the efficiency of these devices depends primarily on their design, operating conditions, and particle size, and that the apparent dependence of efficiency on temperature results from the design of the test system in which the temperature of the particles being tested is not the same as that of the particles being measured. Furthermore, the volatility of typical lubricating oil droplets is such that particles shrink by evaporation during heating and grow by condensation during cooling. The test system uses no dilution, so a dynamic balance exists between the oil droplets and their vapors. Thus, particles passing through the device at elevated temperature are smaller than the particles measured at ambient temperature leading to an apparent shift in the measured size dependent efficiency with temperature.

### 2.1.1 Coalescing Filters

Coalescing filters operate by first capturing particles with the same principles as solid particle filtration; the five collection mechanisms include impaction, interception, diffusion, gravitational settling, and electrostatic attraction. Once liquid droplets are removed from an airflow, coalescence between neighboring drops occurs. Liquid particles that are in close contact overcome surface tension and the particles coalesce into larger drops. As droplets increase in size, gravitational forces become dominant, and the liquid droplets travel to the base of the filter where they further coalesce and drain, or drip, from the bottom of the filter.

Figure 1: Crankcase ventilator assembly. Left to right: coalescing filter attached to lid, housing assembly with silicone tube inlet and outlets

### 2.1.2 Filtration Model

The filtration model described here is based on well established theory and results are not a test of this theory. The model provides a reference case prediction of the temperature dependence of particle filtration. The model is based on single-fiber efficiency

theory (SFE) which was originally developed for dust filtration [12]. Deposition of particle on filter fibers, depends on three processes (excluding electrostatic and gravitation forces – usually ignored): interception, impaction, and diffusion [12, 13]. None of these processes depends upon whether a particle is liquid or solid. The model assumes that when a particle collides with a fiber it sticks, likely a better assumption for liquids than for solids. This is only an approximation for a coalescing filter, where the fibers are coated with liquid films or droplets in dynamic equilibrium between particle deposition, re-entrainment, and drainage. Nevertheless, SFE serves as the base case for predicting coalescing filter performance [13]

Modeling was performed using known and estimated properties of the coalescing filter. Fiber diameter of the filter and filter thickness were known, filter solidity was estimated. Modeling was performed for the same range of temperatures (25-115°C) and filter face velocity (5cm/s) as those used for the test filter. The model assumes the particles and gas are at a uniform temperature, there is no particle bounce, and the filter is a single layer. Not all these assumptions are true for a coalescing filter where liquid particles coalesce and wet the filter during filtration, increasing the effective fiber diameter. However, modeling done with increasing the fiber diameter, within the range one would expect, did not have a significant influence on the predicted filter performance. The model is provided by the University of Minnesota Center for Filtration Research [14] and is based on classical SFE presented in Hinds [12]. Governing equations are described in equations 1-9.

$$E_R = \frac{(1+R)^{-1} - (1+R) + 2(1+1.996Kn)(1+R)ln\,(1+R)}{2[-0.75 - 0.5\ln(\alpha)] + 1.996Kn[-0.5 - \ln(\alpha)]} \qquad (1)$$

$E_R$ is the single-fiber efficiency for interception. R is described in equation 6, Kn is described in equation 5, and α is the filter solidity.

$$E_D = 2.27Ku^{-\frac{1}{3}}Pe^{-\frac{2}{3}}(1 + 0.62Ku^{-\frac{1}{3}}Pe^{\frac{1}{3}}Kn) \quad (2)$$

$E_D$ is the single-fiber efficiency due to diffusion. Pe is described in equation 8.

$$E_{DR} = \frac{1.24R^{2/3}}{(KuPe)^{1/2}} \quad (3)$$

$E_{DR}$ is the interaction term for interception of the diffusing particles.

$$E_I = \frac{Stk^3}{Stk^3 + 0.77Stk^2 + 0.22} \quad (4)$$

$E_I$ is the single-fiber efficiency for impaction. Stk is described in equation 9.

$$Kn = \frac{2\lambda}{d_f} \quad (5)$$

Kn is the Knudson dimensionless number, λ is the mean free path and $d_f$ is the fiber diameter.

$$R = \frac{d_p}{d_f} \quad (6)$$

R is the interception parameter and $d_p$ is the particle diameter.

$$Ku = -\frac{\ln(\alpha)}{2} - \frac{3}{4} + \alpha - \frac{\alpha^2}{4} \quad (7)$$

Ku is the Kuwabara hydrodynamic factor.

$$Pe = \frac{d_f U_f}{D} \tag{8}$$

Pe is the Peclet number, $U_f$ is the filter face velocity and D is the particle diffusion coefficient in air.

$$Stk = \frac{\rho_p {d_p}^2 C_c U_f}{18\eta d_f} \tag{9}$$

Stk is the Stokes number, $C_c$ is the Cunningham slip correction and η is the air dynamic viscosity.

### 2.1.3 Inertial Separator

It was requested that the specific inertial separator device and manufacturer were omitted from publication. The device uses electrically driven rotating disks, subjecting incoming particles to a centrifugal force, throwing them to the walls for subsequent drainage and collection. This makes the removal mechanisms in the inertial separator quite different from the coalescing filter. A detailed removal mechanism model was not investigated. However, diffusion would be expected to dominate removal for small particles and mechanical mobility, the ratio of particle velocity to applied force, in this case inertial, for large particles. The diffusion coefficient and mechanical mobility, B, of particles given by Hinds [12] are:

$$D = kTB \tag{10}$$

$$B = \frac{C_c}{3\pi\eta d_p} \tag{11}$$

Where k is Boltzmann's constant.

Both diffusion coefficient and mechanical mobility are temperature dependent. For example, a 0.5μm particle in air, increasing temperature from 25 to 115°C increases the diffusion coefficient by 16% and decreases the mechanical mobility by 11%. This change in diffusion coefficient is equivalent to shifting the particle size from 0.5 to 0.47μm and the change in mechanical mobility is equivalent to changing the particle size from 0.5 to 0.52μm (inertial force proportional to $d_p^3$). Thus, one would expect very modest changes in the shapes of the fractional efficiency plots resulting from changes in diffusion coefficient and mechanical mobility in this temperature range.

### 2.1.4 Particle Evaporation and Condensation

Changes in particle size due to evaporation and condensation were modeled based on the volatility of normal alkanes. For simplicity, particle constituents were assumed to behave as separate droplets, rather than a mixture. Calculations were done for C20, C24, and C28 normal alkanes. The governing equation for change in particle size per unit time is equation 12 below and the evaporation time is equation 13.

$$\frac{d(d_p)}{dt} = \frac{4D_v M}{R\rho_p d_p}\left(\frac{P_\infty}{T_\infty} - \frac{P_d}{T_d}\right)(\phi) \tag{12}$$

$$t = \frac{R\rho_p {d_p}^2}{8D_v M}\left(\frac{P_d}{T_d} - \frac{P_\infty}{T_\infty}\right) \tag{13}$$

Where $D_v$ is the diffusion of the alkane vapor in air, R is the gas constant, $P_\infty$ is the partial pressure of vapor well away from the drop, $T_\infty$ is the temperature far from the droplet, $P_d$ is the partial pressure on the surface of the droplet, $T_d$ is the droplet temperature and $\phi$ is the Fuchs correction factor, which is equal to 1 in the size range considered here. No correction was made for the Kelvin effect.

In the case of evaporation, it is assumed that the partial pressure of vapor far from the droplet, $P_\infty$, is equal to zero. For particle growth, the partial pressure of the vapor far from the droplet, $P_\infty$, is assumed to be equal to what the partial pressure was at the droplet surface, $P_d$, during evaporation. During evaporation, it is assumed that the particles shrink until they come to an equilibrium where the partial pressure of the vapor far from the droplet is equal to the saturation vapor pressure. The assumptions made in these evaporation and condensation models are approximations, but they should be sufficiently accurate to determine the plausibility of significant particle shrinkage while at high temperature followed by regrowth as the particle is cooled to ambient conditions.

## *2.2 Objectives*

The primary objective of this project was to determine the influence of temperature on the performance of systems designed to remove particles from crankcase fumes and similar aerosols. The matter was introduced when a concerning trend in decreasing filtration efficiency of CV devices was found by Cummins Filtration in Stoughton, WI when developing ISO procedures for CV filter, laboratory-based test standards. The T. E. Murphy Engine Research Lab was approached to act as a blind study participant, building

a CV device test apparatus and measurement system without the expected results disclosed. The ensuing, secondary objective was to further investigate and classify the cause of particle penetration changing in coalescing filters at elevated temperatures. The findings from this project have implications in our understanding of the processing of semi-volatile particles in emission control devices that operate over a range of temperatures, such as crankcase ventilation systems for cars and trucks in the light to heavy duty markets.

## *2.3 Apparatus Design*

The apparatus was designed to perform under conditions representative of a typical engine bay. The key parameters were operation temperature from ambient to a maximum of 115 °C and flow rates up to 300 SLPM which corresponds to a 10 cm/s face velocity for the coalescing filter.

The crankcase ventilation aerosol removal device testing was designed to meet ISO 17356-4 requirements for CV laboratory based fractional efficiency testing [15]. A set of requirements were also prepared for the system to measure aerosol particles with stability, accuracy, and without bias. The requirements can be broken down into three main considerations: flow development, an isothermal test system, and sampling practices.

When considering flow development, it was preferred that the oil aerosol and dilution air would encounter geometry changes to promote mixing. Along with geometry changes, it was ensured there would be a straight tube length of, at minimum, 10 diameters prior to sampling ports. This was to avoid the possibility of sampling in a poorly mixed region.

The second set of considerations were in respect to devising an isothermal system. This was desired to ensure oil and gas properties were constant from a pre-filtration sample port, across the filtration medium, and up to a post-filtration sampling port. The least complex solution would be encasing the entire test system within an oven. This was not an option due to cost and space limitations. Instead, the apparatus was wrapped in sections of heat tape and insulation. The CV filter housings were irregularly shaped and not appropriate for wrapping with heating tape or insulation. A 76L oven was retrofitted to mount entire CV devices inside. Holes were cut into the oven wall on opposing sides for an inlet and outlet pipe connected to the CV.

The third and final consideration was implementing a low-loss sampling system that minimized size dependent sampling errors. The first application was the use of carbon impregnated silicone tubing for aerosol sample transport between the apparatus and measurement instruments. Flexible plastic tubes, such as Teflon™, are susceptible to producing an electric field inside of the tubing [16]. If charged particles are transported using such tubing, electrostatic losses are significant, thus Teflon™ tubing was avoided in favor of carbon impregnated silicone tubing. The second practice implemented was the use of isokinetic sampling. Isokinetic sampling is defined as having the velocity of particles entering a sample probe ($V_{sample}$) equal to the velocity of the bulk aerosol flowing ($V_{flow}$) past the probe. If the sampling velocity is greater than the bulk flowing aerosol ($V_{sample} > V_{flow}$), larger particles will be under-sampled. Streamlines are pulled in toward the sample probe for this case and the larger particles are unable to follow the bending streamlines due to their inertia; the large particles break from their original streamline and travel past the sample probe, whereas smaller particles tend to follow the streamlines. If the sampling

velocity is less than the bulk flowing aerosol ($V_{sample} < V_{flow}$), larger particles will be over-sampled. For this case streamlines are being driven around the sample probe. Smaller particles follow the streamlines around the sample probe while larger particles with sufficient inertia will diverge from the streamline and enter the sample probe. See figure 2 for an illustration of sampling streamlines and generalized biases related to having non-isokinetic conditions.

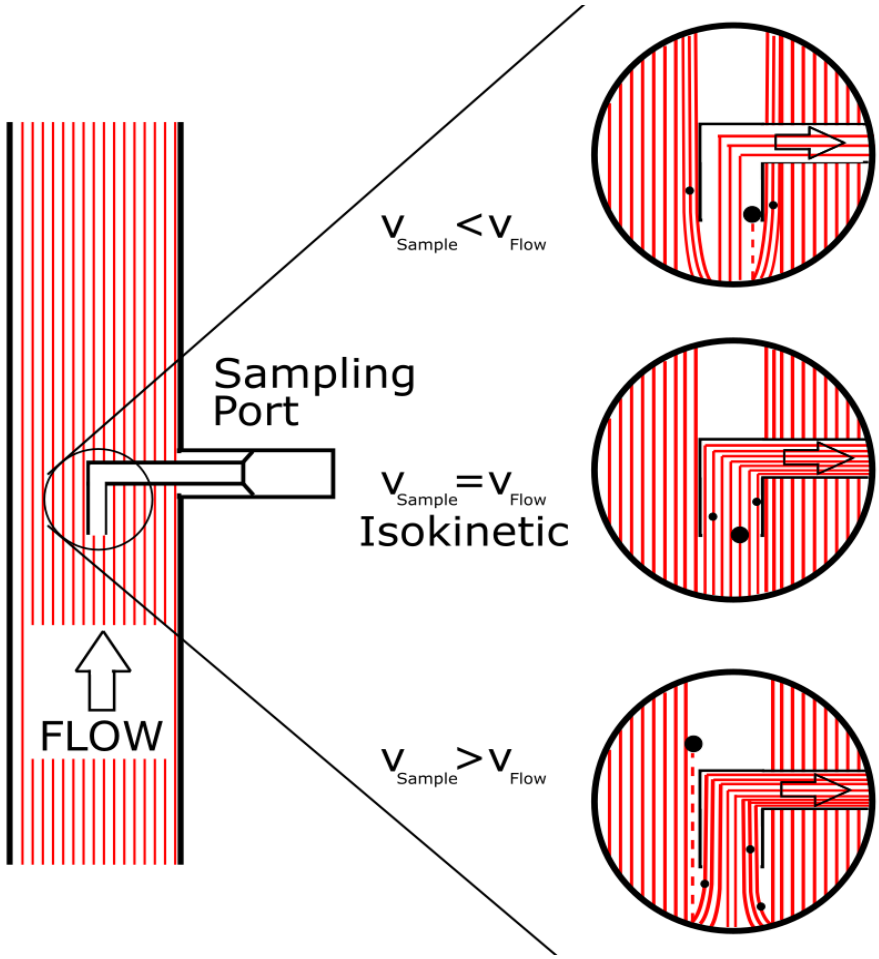


Figure 2: Isokinetic versus non-isokinetic sampling biases

## *2.4 Test Bench and Instrumentation*

The following section is a description of the instrumentation and devices used in the filter testing apparatus constructed for this project at the University of Minnesota, Murphy Engine Research Laboratory. Figure 3 below is a process and instrument diagram depicting each component with a reference number allotted in Table 1. The reference number, component and manufacturer, usage in the test system, and operating parameters, are described in Table 1 below. The crankcase ventilation aerosol removal device testing apparatus was designed to meet ISO 17356-4 requirements for CV laboratory based fractional efficiency testing [15].

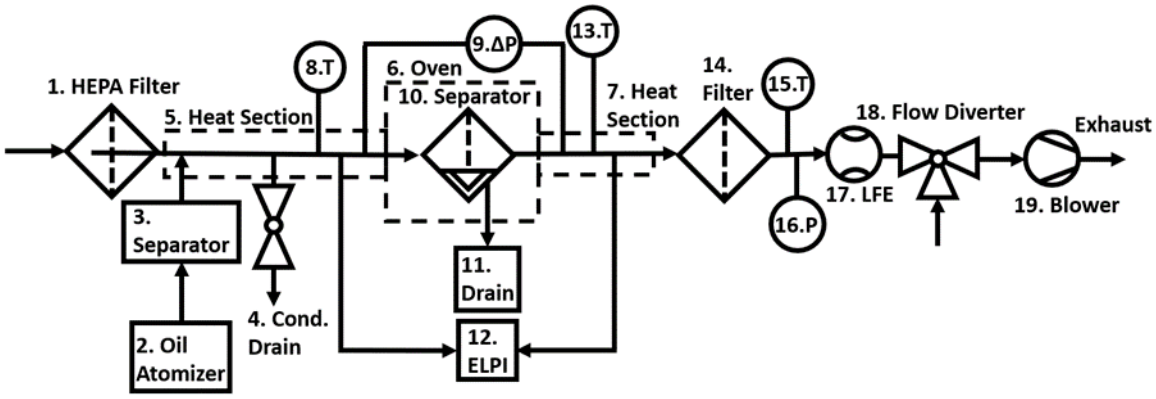


Figure 3: Aerosol separator laboratory fractional efficiency test setup

Table 1: Instruments, manufacturers, and device parameters of operation

| Ref. # | Instrument<br>———<br>Manufacturer | Usage | Parameters of Operation |
|---|---|---|---|
| 1 | HEPA Filter<br>———<br>Donaldson Ultra™ Filter P194410 | Provides the clean dilution air to the carry the test aerosol. Flow varied to meet filter face velocity target. | Filtration efficiency of 99.97% at 0.3 [um]. Operated at Q=225 [L/min] ΔP=0.2 [inH2O] at |
| 2 | Oil Atomizer<br>———<br>Palas PLG 2100 Atomizer | Operates with the Laskin nozzle process. The atomizer is used to create a polydisperse aerosol of liquid oil droplets resembling a crankcase fume. | Volumetric flowrate of 9.1 [L/min]. Liquid reservoir heated to 110 [°C]. Aerosol particle size from 0.08→3 [μm] produced by chosen oil with D50≅0.5 [μm]. The atomizer was supplied purified, compressed air at 20[psi]. |
| 3 | Inertial Separator<br>———<br>In-house, custom manufactured product | Remove larger particles that are expected to settle within the system, therein preventing oil buildup throughout. It is placed downstream to, and physically above the atomizer to allow gravity induced flow back to the atomizer's liquid reservoir. | Cut-size unspecified. Designed for operating with PLG 2100 atomizer with flowrate near 10 [L/min]. |
| 4 | Condensation Drain<br>———<br>Glacier Tanks LLC, B7MP-G200 Long Tee Tri Clamp 2in | A secondary location for accumulating larger particles that settle after experiencing turbulence from the filtered air and atomized oil mixing. Oil gravitationally settles to the pipe perpendicular to main flow. The tee has a reducer and 1/4"[in] plug can be manually removed to drain oil collected. | Standard 304 stainless steel 2 [in] sanitary piping, tee fitting from Glacier Tanks |
| 5, 7 | Heating Sections<br>———<br>Briskheat 830[W] heat tape strips. Omega CN401 PID Controller | The system is comprised of three independent heating sections, reference # 5, 6, and 7 shown in figure 3. Number 5 is split into halves where the upstream half is heated above goal temperature. The latter half of component 5, as well as parts 6 and 7 have the flow temperature set to the desired aerosol temperature. The aerosol enters the second half of part 5 at or near the setpoint temperature, hence it maintains an isothermal setpoint aerosol temperature with minimal temperature gradient | Controlled by PID controller to heat oil mist and air mixture to maximum temperature of 115°C, except for the first half of section 5 which is overheated by approximately 10%. |

| | | | |
|---|---|---|---|
| | | throughout the filtration and sampling regions. | |
| 6 | Oven<br>———————<br>Refurbished product, unknown manufacturer | Repurposed oven that has been modified to hold a variety of filtration housings. Sanitary piping breaches through the right and left walls to connect the chosen filtration housing in-line with the aerosol flow system. The oven is controlled with an OMEGA temperature controller and contains a 110V fan for instigating convective temperature homogeneity. | Internal dimensions of 16x12x24 [in]. Maximum temperature (attempted) of 150[°C]. Temperature stability after reaching set temperature: ± 2[°C] after 5 minutes, ± 0.1[°C] after 20 minutes. Maximum temperature differential between top and bottom of the oven of up to 4[°C] when the setpoint was 115[°C]. |
| - | Isokinetic Tips<br>———————<br>In-house custom manufactured product | Placed on each of the sampling ports, one upstream of the CV device, and one downstream to achieve isokinetic sampling. | Friction fit onto ¼ [in] sampling lines. The tips extend from the sampling inlets and modify the diameter to achieve an isokinetic particle sampling velocity. Eight[mm] isokinetic tips were used. |
| 8, 13, 15 | Thermocouple<br>———————<br>Omega K-type | Measuring flow temperature at sample point to ensure it is at target temperature. | Measuring temperature from 20-115[°C]. |
| 9 | Differential Pressure Transmitter<br>———————<br>Omega PX409-001DDU5V | Measuring the pressure drop across equipped aerosol separator device. | Operated from 0-10[inH2O] (0-0.36[psi]) |
| 10 | Oil Aerosol Separator Device<br>———————<br>Various | This is the device being tested. This will either be a coalescing filter or inertial separator device. | Operated at 5cm/s face velocity for coalescing filters. Flowrate was matched for inertial separator. |
| 11 | Oil Drain<br>———————<br>In-house Product | Used to gravimetrically collect and temporarily store oil draining from the separator device of choice during testing. | Oil collection was dependent on removal device. Maximum collection rate observed was 10[g/hr] of oil. |
| 12 | Electric Low-Pressure Impactor (ELPI)<br>——————— | A low-pressure impactor used for number-based particle size measurement. It consists of a corona charger followed by a 13-stage cascade impactor. From the Dekati | Operated at 10[L/min]. Measuring with largest current range possible of 400,000[fA]. Operating under 100[mbar] of |

| | | | |
|---|---|---|---|
| | Dekati | product brochure [17]: "*All the impactor stages are electrically insulated from each other and each of the impactor stages is connected to an electrometer. As the charged particles get collected in the different impactor stages, the charge carried by them is detected by the electrometers. This measured current signal is directly related to the number of particles, thus enabling the ELPI® to measure particle number size distribution and concentration in real-time*". Sizing is based on particle aerodynamic diameter; the charging is based on Stokes diameter. | pressure in the final, smallest cut stage. The D50 cutoff sizes, in microns, of the 13 stages from largest to smallest are: 8.0953, 5.1766, 3.2085, 2.0422, 1.2999, 0.8178, 0.5163, 0.3296, 0.2149, 0.1373, 0.0829, and 0.0435. Please note that the largest and smallest particle sizes in this distribution may not be included in graphical results due to the very low particle concentrations. The low concentrations are often near the limits of detection and are not able to be measured with repeatability. |
| 14 | Absolute Filter<br>———<br>Unknown manufacturer | Filter liquid particulate entrained in the aerosol. Post-filtration air is suitable for exhausting inside of a populated test cell. | Diameter of 24[in]. Pressure drop of 1 [inH2O] (clean) at Q= 150 [L/min]. |
| 16 | Differential Pressure Transmitter<br>———<br>Omega PX409-001DDU5V | Measuring the difference between vacuum on the blower inlet side, and ambient pressure. Reference for replacing item #14, the absolute filter. | Operated from 0-25 [inH2O] (0-0.90[psi]) |
| 17 | Laminar Flow Element<br>———<br>Meriam, 50MW20-2 Laminar Flow Element. | Flow rate measurement device for test bench. | Maximum flowrate of 1130 [L/min] at $\Delta P$ = 8[in$H_2O$]. Operated near 150 [L/min]. |
| 18 | 3-Way Valve<br>———<br>Unknown manufacturer | Connected to blower for manual flowrate adjustment of test bench, where 3-way valve adjustment pulls more from test bench to increase flowrate or pulls from the surrounding air instead. | Majority of flow was directed from the test bench side |
| 19 | Blower<br>———<br>Unknown manufacturer | Operates at constant flowrate. Provides vacuum to draw aerosol through the test bench. | Capable of 250[SLPM]. System flowrate dependent on test filter media condition and exhaust filter condition. |

| | | | |
|---|---|---|---|
| - | DAQ Chassis and Modules<br>———————<br>NI cDAQ 9174<br>NI 9213<br>NI 9215 | 9174 is a compact DAQ chassis designed to operate up to four modules simultaneously through one USB connection. NI 9213 is a module for input and conversion of thermocouple signals.<br>NI 9215 is a module for collecting analog voltage signals, used here for logging pressure transmitter data. | Individual data points collected as an average of 100 samples captured at 100Hz. |

## *2.5. Lubricating Test Oils*

Four test lube oils were used in this study: a standard commercially available 15W-40 oil common to compression ignition applications, a high volatility custom blend with similar viscosity characteristics, a low volatility custom blend with similar viscosity characteristics, and a low volatility vacuum pump oil. Test oil specifications included density, surface tension, and viscosity from 40-100°C and Noack evaporation at 250°C. A summary of the properties is shown in Table 2 below.

Table 2: Properties of lubricating oils used in study

| Density ($g/cm^3$) | | | | |
|---|---|---|---|---|
| Temp. | Standard 15W-40 | High Vol. 15W-40 | Low Vol. 15W-40 | Vacuum Pump Oil |
| 40°C | 0.85 | 0.84 | 0.81 | 0.82 |
| 80°C | 0.83 | 0.81 | 0.78 | 0.79 |
| 100°C | 0.81 | 0.80 | 0.77 | 0.78 |

| Surface Tension (mN/m) | | | | |
|---|---|---|---|---|
| Temp. | Standard 15W-40 | High Vol. 15W-40 | Low Vol. 15W-40 | Vacuum Pump Oil |
| 40°C | 25.31 | 29.35 | 28.03 | 28.45 |
| 80°C | 23.21 | 25.98 | 25.19 | 25.89 |
| 100°C | 22.04 | 24.74 | 23.66 | 24.17 |

| Dynamic Viscosity (Pa s) | | | | |
|---|---|---|---|---|
| Temp. | Standard 15W-40* | High Vol. 15W-40 | Low Vol. 15W-40 | Vacuum Pump Oil |
| 40°C | 0.037 | 0.035 | 0.027 | 0.043 |
| 80°C | 0.009 | 0.009 | 0.008 | 0.012 |
| 100°C | 0.006 | 0.006 | 0.005 | 0.008 |

* Dynamic viscosity from another (but similar) 15W-40 that was not used in study.

| Noack TGA Evaporation Percent [%] at 250°C | | | |
|---|---|---|---|
| Standard 15W-40 | High Vol. 15W-40 | Low Vol. 15W-40 | Vacuum Pump Oil |
| 8.4-11 | 16.6 | 6.4 | 1.3 |

## *2.5 Operating Procedure*

The test bench was operated in a procedural manner wherein the steps listed below were followed for each test. This was in effort to minimize uncertainty associated with operator error. Steps 1-10 with bulleted form description are listed below.

1. Prepare Atomizer
    i. Weigh oil
    ii. Refill oil to 2.736 kg
    iii. Turn on and regulate pressure until it settles at 20psi
2. Setup Temperature Monitoring
    i. Turn on data acquisition hardware
    ii. Launch LabView software program on laptop
3. Turn on Heating Elements (Unless running at ambient temperature)
    i. Turn on all heat tapes and set to predetermined temperatures
    ii. Turn on oven and set to desired temperature
4. Turn on Blower
    i. Ensure that the pressure drop across the LFE corresponds to the desired flow rate and monitor downstream pressure to ensure the outlet filter is clean
5. Stabilization Period
    i. Wait until all monitored temperatures oscillate within 0.5C, this takes approximately 15 minutes. Adjust heat tape and oven temperature setpoints as necessary.
    ii. Wait for the filter to be saturated by observing a stagnation in pressure drop increase, accompanied by oil dripping from the bottom of the filter housing.

iii. Ensure that the pressure drop across the LFE corresponds to the desired flow rate, given the increase in flow temperature at LFE.

6. Preparing the ELPI
    i. Turn on the ELPI while a HEPA filter is attached
    ii. Turn the charger on
    iii. Remove the hepa filter and turn the flush pump on
    iv. Launch the ELPI IV program and begin the zeroing process
    v. Turn the flush pump off
7. Measurement
    i. Begin saving data on the ELPI IV program
    ii. Open the switching valve for the sampling ports to the downstream position
    iii. Attach the ELPI to the monitor stream
    iv. Allow 30 seconds for currents to stabilize
    v. Allow for 60 seconds of data collection
    vi. Switch the valve to the upstream position and follow the previous two steps
    vii. Disconnect the ELPI and stop saving data
    viii. Close the switching valve
8. Transition to Another Measurement
    i. Clean the ELPI
    ii. Set temperatures to desired value and repeat step five
9. Finishing Operation
    1. Power off all components and allow for cooling of apparatus
10. Data Analysis

i. Filter data into an excel file using ELPI IV program

ii. Copy each 60 second measurement into a separate excel file

iii. Proceed with analysis

## *2.6 Results and Discussion*

Figures 4-8 present the fractional efficiency curves of the coalescing filter for four different test oils plotted against temperature. For clarity, individual data points are not shown, and the curves are smoothed fits through the data points. The coalescing filter was tested at a face velocity of 5cm/s for all results shown. The rotating inertial separator was operated at the same system flow rate as the coalescing filter, 150 LPM.

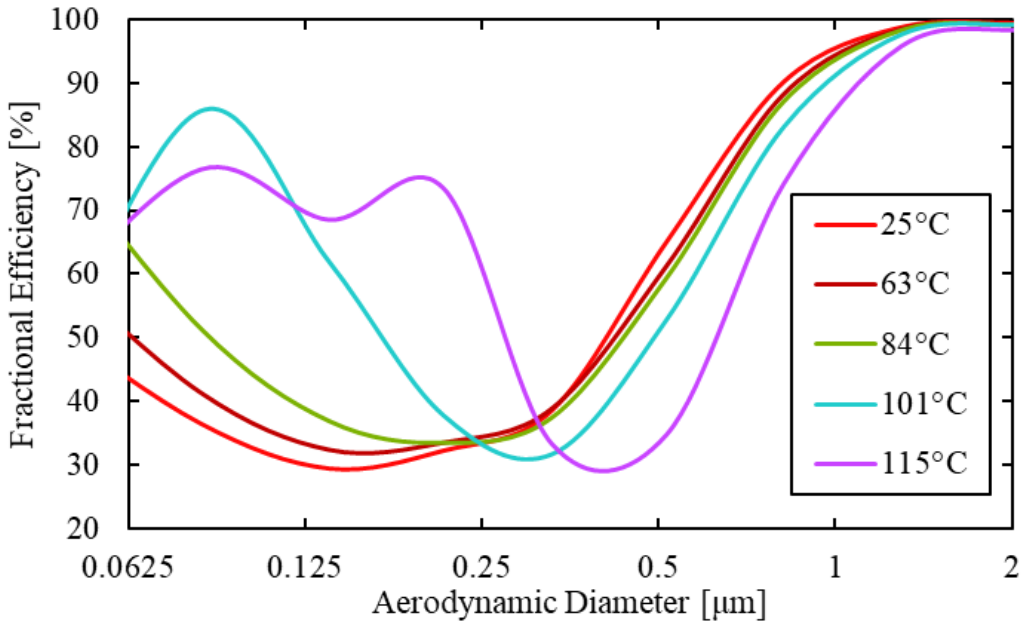


Figure 4: Fractional removal efficiency of coalescing filter versus temperature, standard 15W-40 oil.

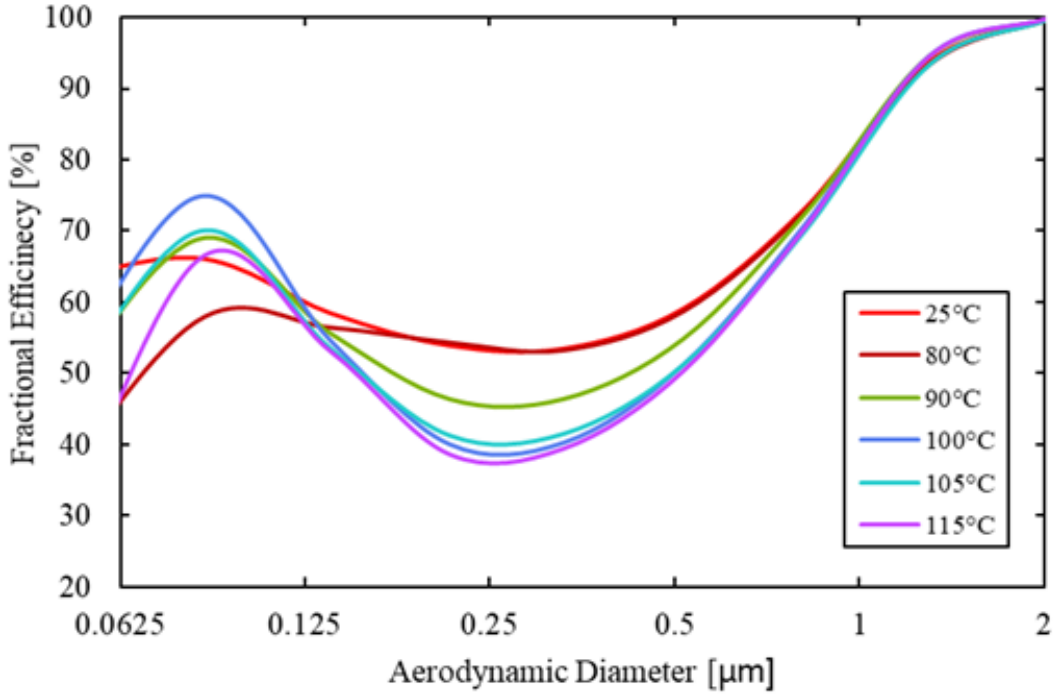


Figure 5: Fractional removal efficiency of coalescing filter versus temperature, synthetic vacuum pump oil

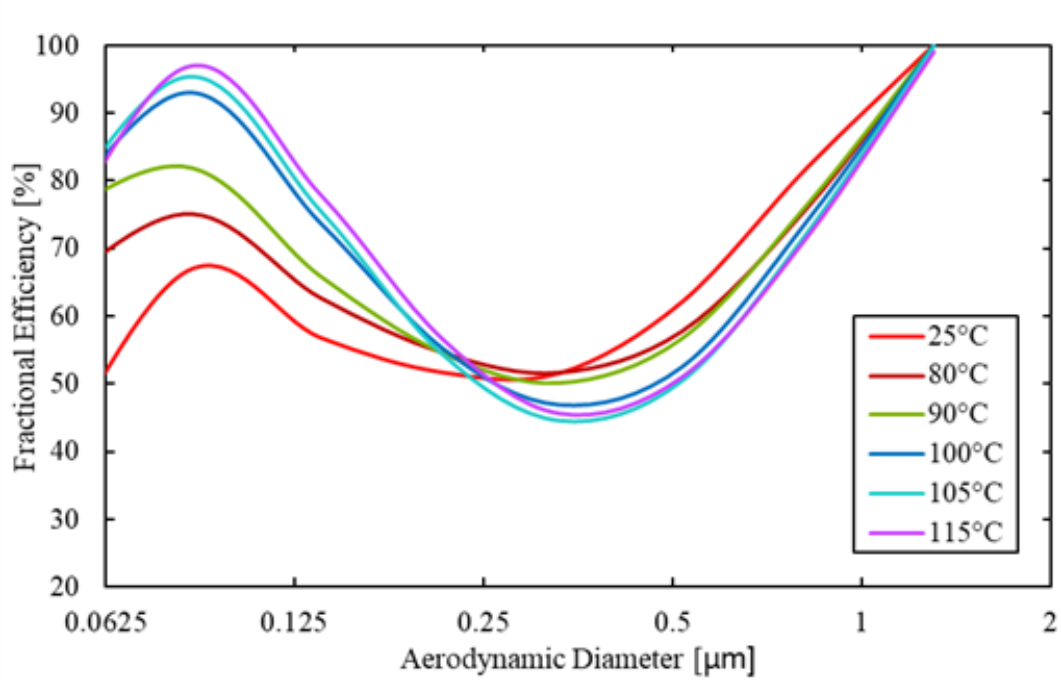


Figure 6: Fractional removal efficiency of coalescing filter versus temperature, low volatility 15W-40 oil

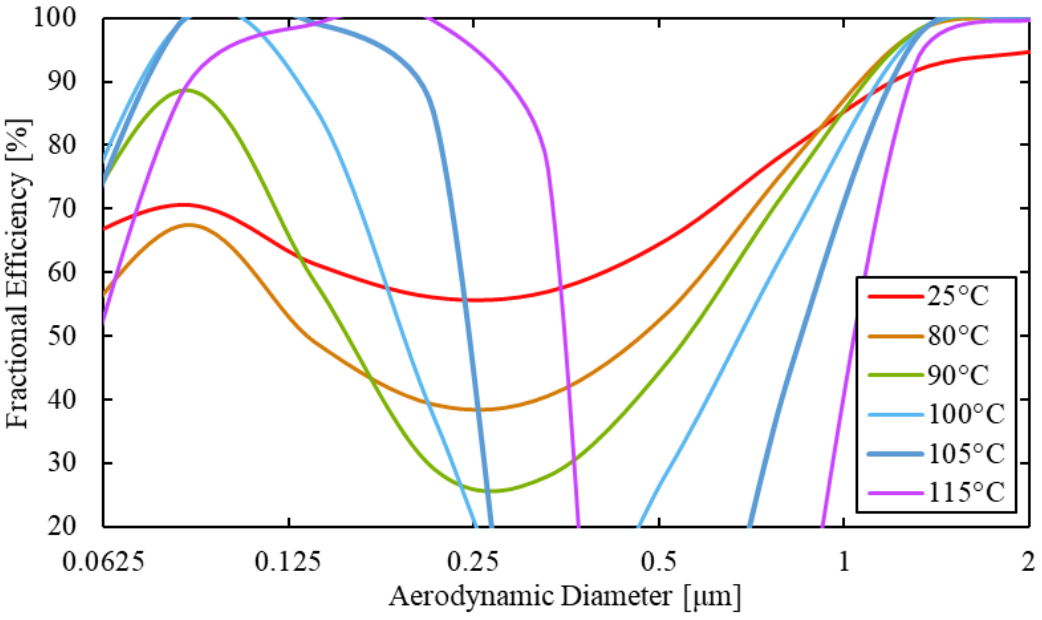


Figure 7: Fractional removal efficiency of coalescing filter versus temperature, high volatility 15W-40 oil

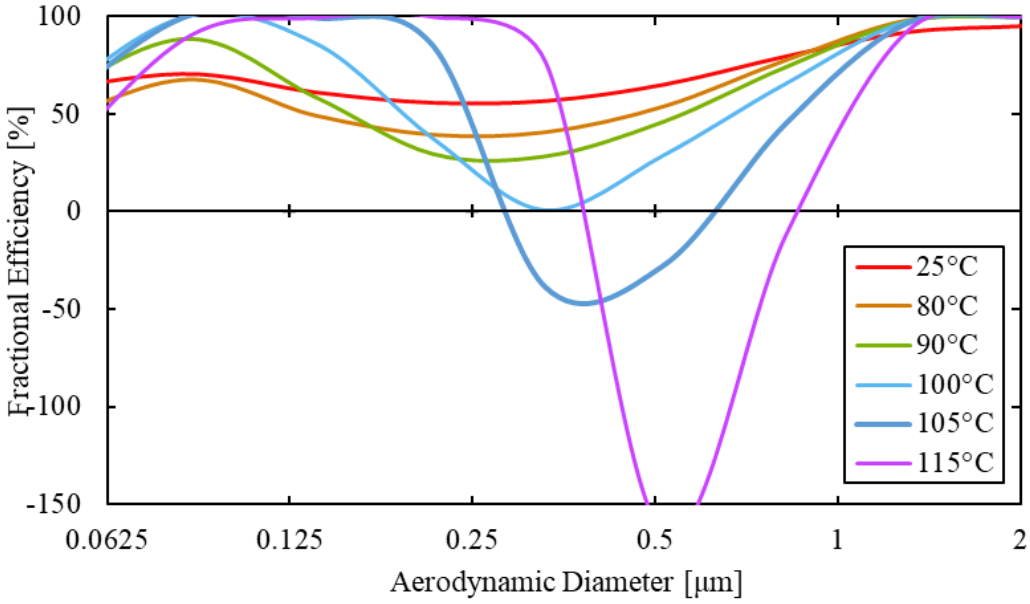


Figure 8: Fractional removal efficiency of coalescing filter versus temperature, high volatility 15W-40 oil. Y-axis expanded from standard format

Figure 4 shows the influence of temperature on the fractional removal efficiency of the coalescing filter using a standard 15W-40 test oil. The MPPS is approximately 0.15μm at 25°C and shifts continuously with increasing temperature to about 0.41μm the highest temperature, 115°C. Figures 5 and 6 show corresponding results for the vacuum pump oil and the low volatility 15W-40 oil. With vacuum pump oil (very low volatility) there is little change in the MPPS, but a substantial decrease in filtration efficiency with increasing temperature. The low volatility 15W-40 engine oil shows a modest shift in MPPS to larger size with increasing temperature. Figure 7 presents the high volatility oil results, where a dramatic decrease in MPPS efficiency is seen with increasing temperature. The efficiency equates to an apparent negative fractional filtration efficiency which is better seen in Figure 8 where the Y-axis is expanded from the standard axis limits used among all other fractional efficiency plots. When the concentration of particles in a size bin is greater downstream than upstream the calculated filtration efficiency is negative, which indicates particle creation. Reasons for this may provide valuable insight to the other test conditions where this is not observed, possibly because the effects are not as prominent. This will be further discussed near the end of this subsection.

Figures 9-12 show fractional efficiency curves for the rotating inertial separator using the same four test oils.

Figure 9 shows a large shift in MPPS with increasing temperature for the standard 15W-40 test oil. This is like the coalescing filter result with the same test oil in figure 4, even though the rotating inertial separator operates with different removal mechanism.

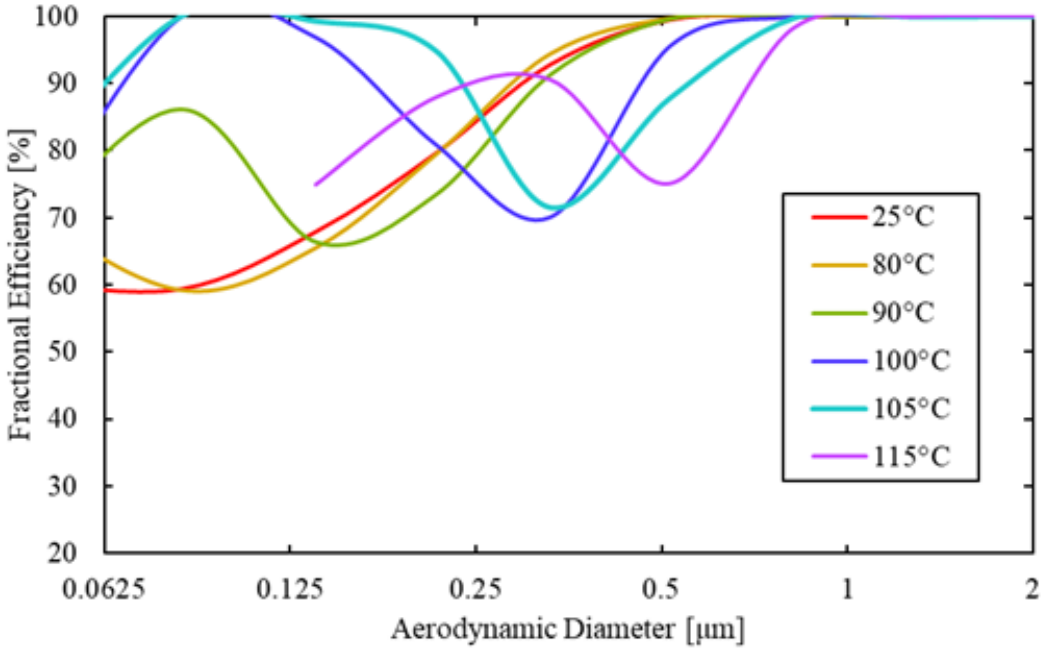


Figure 9: Fractional removal efficiency of rotating inertial separator versus temperature, standard 15w-40 oil

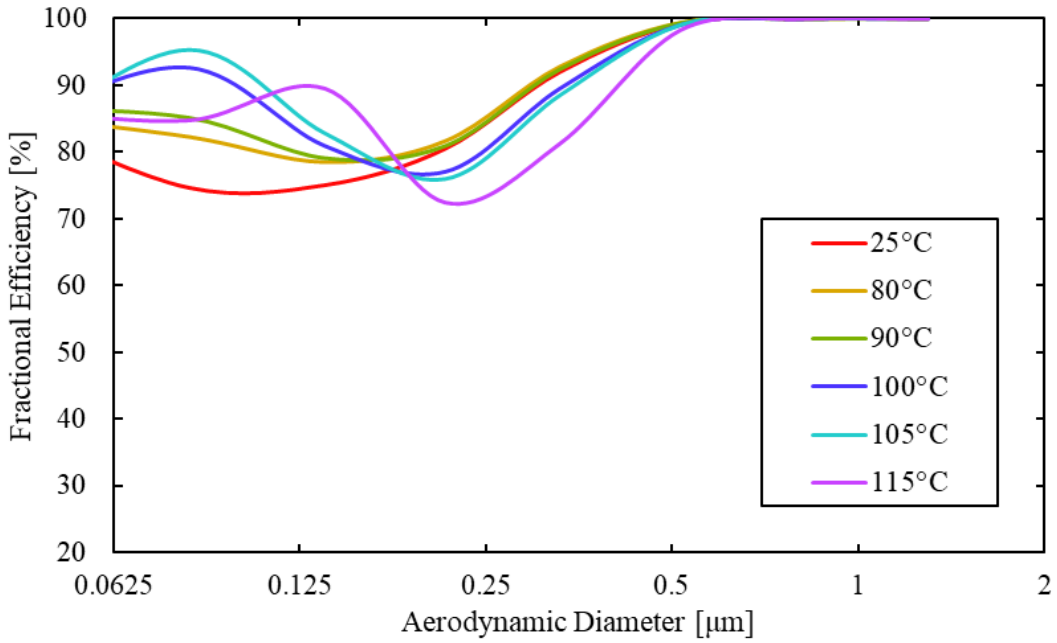


Figure 10: Fractional removal efficiency of rotating inertial separator versus temperature, synthetic vacuum pump oil

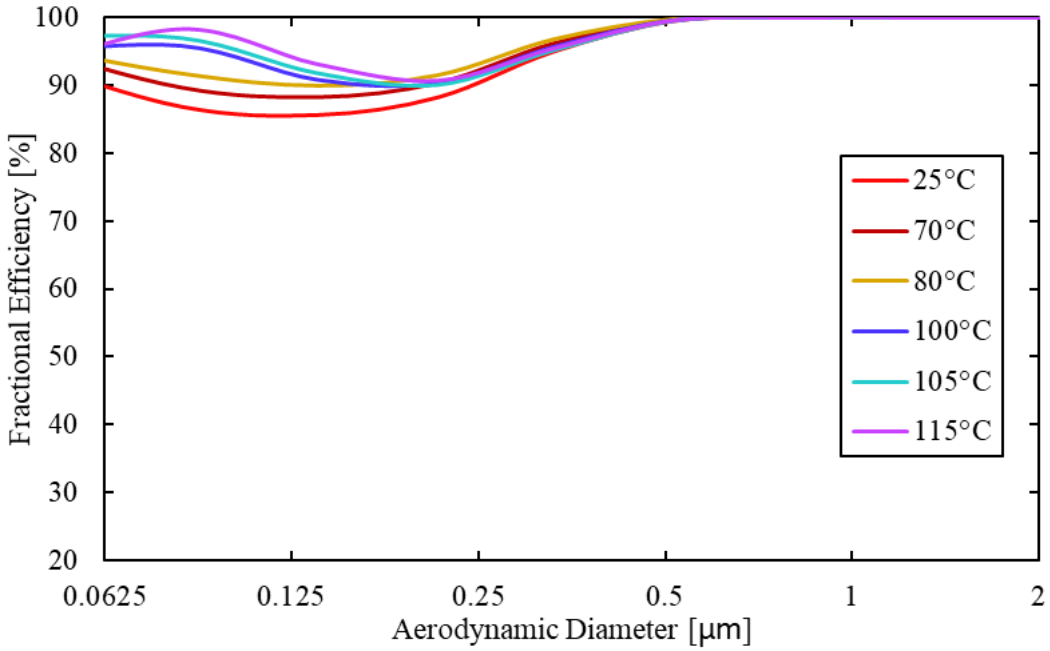


Figure 11: Fractional removal efficiency of rotating inertial separator versus temperature, low volatility 15W-40 oil

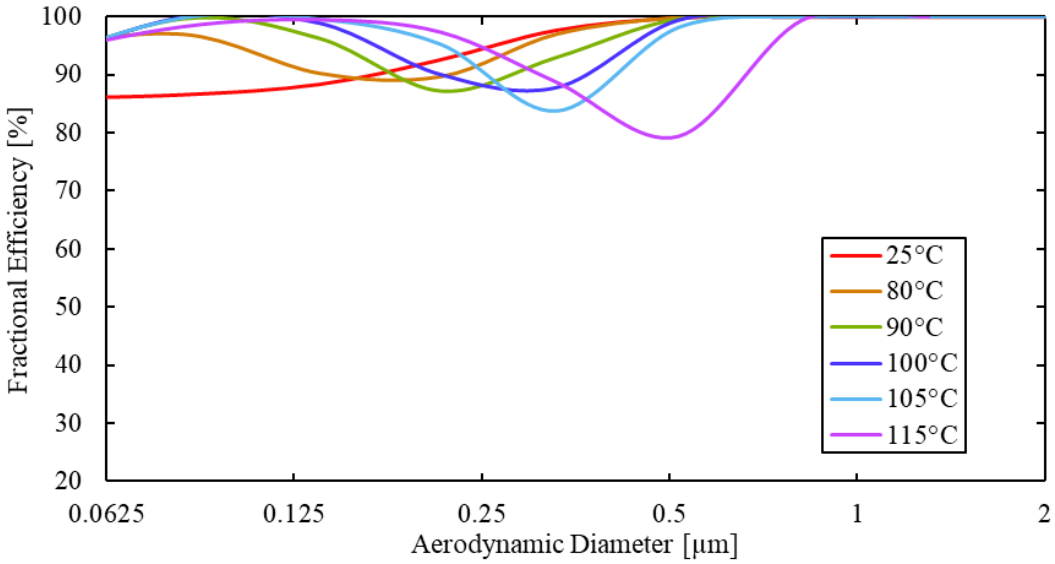


Figure 12: Fractional removal efficiency of rotating inertial separator versus temperature, high volatility 15W-40 oil

Figure 10 shows the fractional efficiency plot for the inertial separator using vacuum pump oil particles. The results are different from those using the same test oil with the coalescing filter shown in figure 5. With the coalescing filter, increasing temperature decreased the efficiency at the MPPS but the MPPS did not shift, on the other hand, with the inertial separator the MPPS shifts to larger size but there is only a modest change in efficiency. Reasons for this behavior are unclear.

Figure 11 shows the fractional efficiency plot for the inertial separator using the low volatility 15W-40 engine oil. Here, temperature has a very modest impact with MPPS shifting slightly to larger particles and efficiency at MPPS increasing slightly as temperature increases.

Figure 12 shows the fractional efficiency plot for the inertial separator using the high volatility 15W-40 engine oil. Temperature has a great impact on the MPPS shifting to larger diameter with increasing temperature, mimicking the MPPS shifts with regular 15W-40 oil. Efficiency at the MPPS decreases with increasing temperature.

To summarize, for both removal devices, and for each of the test oils, standard 15W-40, vacuum pump oil, and specially formulated high and low volatility 15W-40 mixes, the shape of the fractional efficiency curve changes with temperature, with the MPPS shifting to larger sizes as temperature increases. The changes were much more modest with the low volatility oil. These shifts are not predicted by theory. The results were inconsistent for the synthetic vacuum pump oil for reasons that are unclear. Further understanding in the synthetic vacuum pump oil aerosol testing, and each of the oils for that matter, can be investigated through additional testing suggested and discussed in section 2.7. The high volatility oil has a distinct shift of MPPS to larger diameters with increasing temperature,

but the results with the coalescing filter were compromised by particle formation at the highest temperature. On the other hand, the inertial separator showed a clean temperature dependence with no evidence of particle formation.

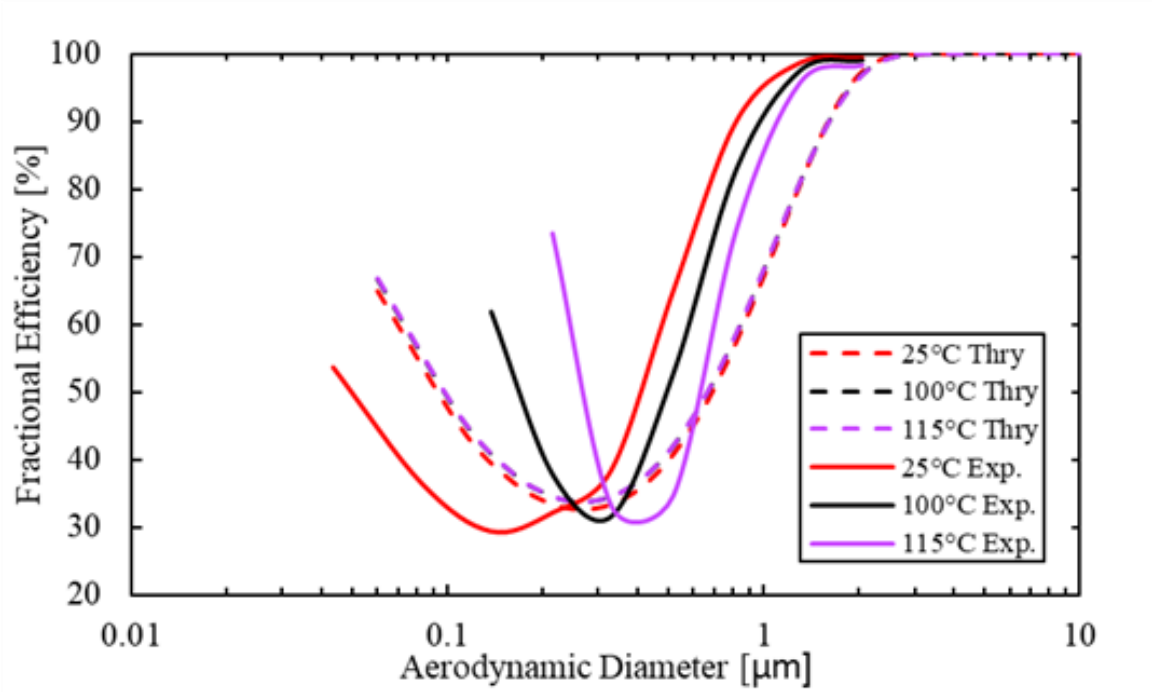


Figure 13: Fractional removal efficiency of coalescing filter versus temperature for theoretical model and experimental data, standard 15W-40 test oil

In figure 13, experimental fractional efficiency curves are compared with results of the filtration model. The experimental results show significant shifting of the efficiency curves with temperature, while the model results lie essentially on top of one another for this temperature range. Figure 14 presents these results in a different way. Here MPPS is plotted against versus temperature for the theoretical and standard 15W-40 experimental results. The MPPS can be seen shifting with temperature for experimental results, but not predicted in the theoretical values shown in figures 7 and 13.

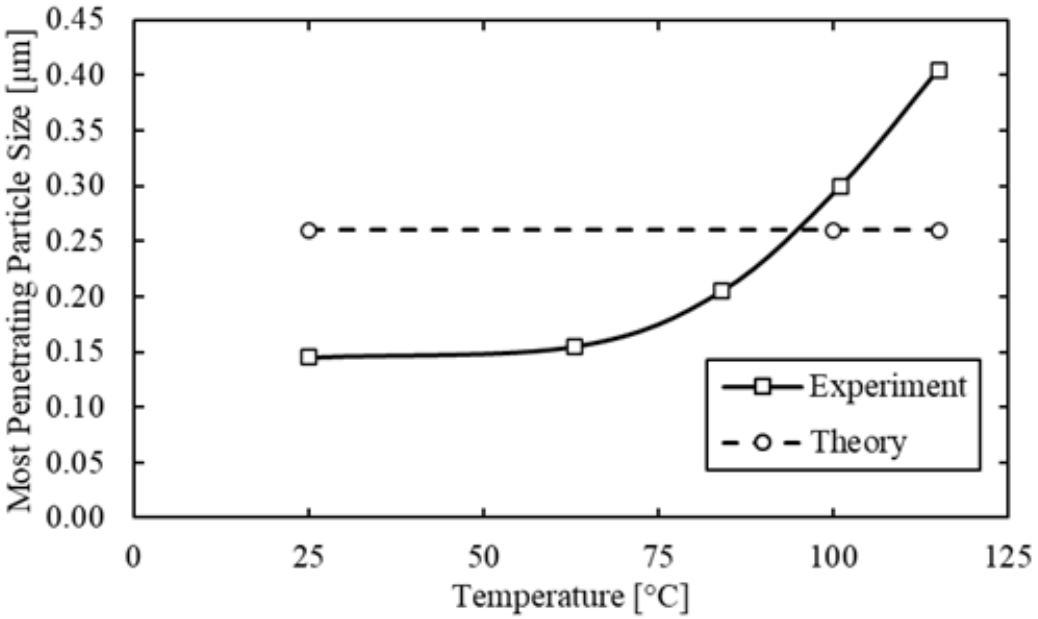


Figure 14: Most penetrating particle size versus temperature for the theoretical model and experimental data, standard 15W-40 test oil

An analysis of changes in the measured upstream and downstream distributions with temperature provides additional insights. Figure 15 shows typical upstream mass and number weighted size distributions, standard 15W-40 test oil at 25°C. Also shown is a lognormal fit to the number distribution. The stability of the upstream test aerosols used in the coalescing filter tests is shown in Figure 16-18. Figure 16 is a plot of upstream number and mass concentrations against temperature, figure 17 fitted upstream number size distributions over temperature range, and figure 18, parameters of the fitted distributions, geometric mean diameter, GMD, and geometric standard deviation, $\sigma_g$, plotted against temperature. There are only modest changes in mass and number concentrations and size distribution parameters over a wide temperature range. These changes are likely due to the variation in the behavior of the atomizer. On the other hand, the characteristics of the

downstream size distribution are strongly influenced by temperature as seen in figures 19 and 20.

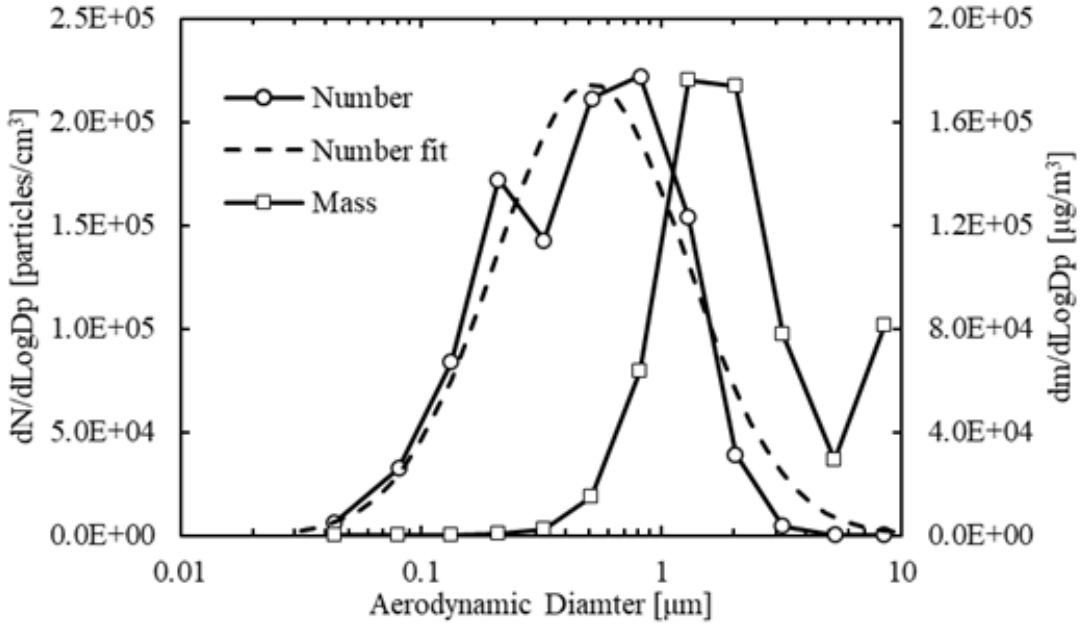


Figure 15: Mass, number, and number fit upstream distributions for base case 25°C

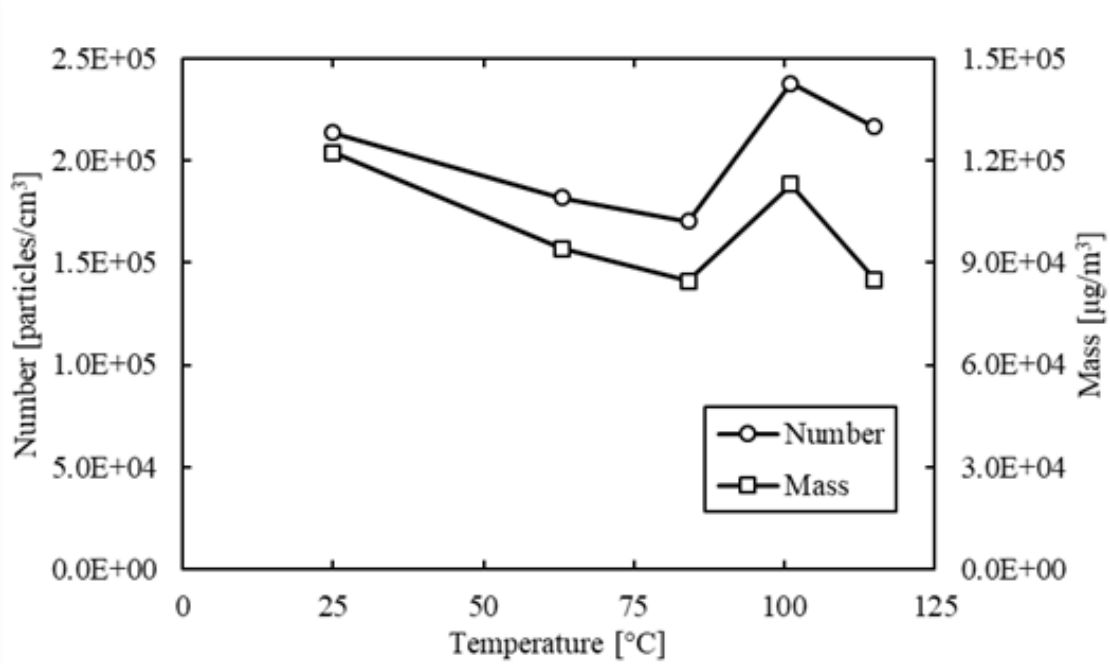


Figure 16: Total upstream mass and number concentration versus temperature

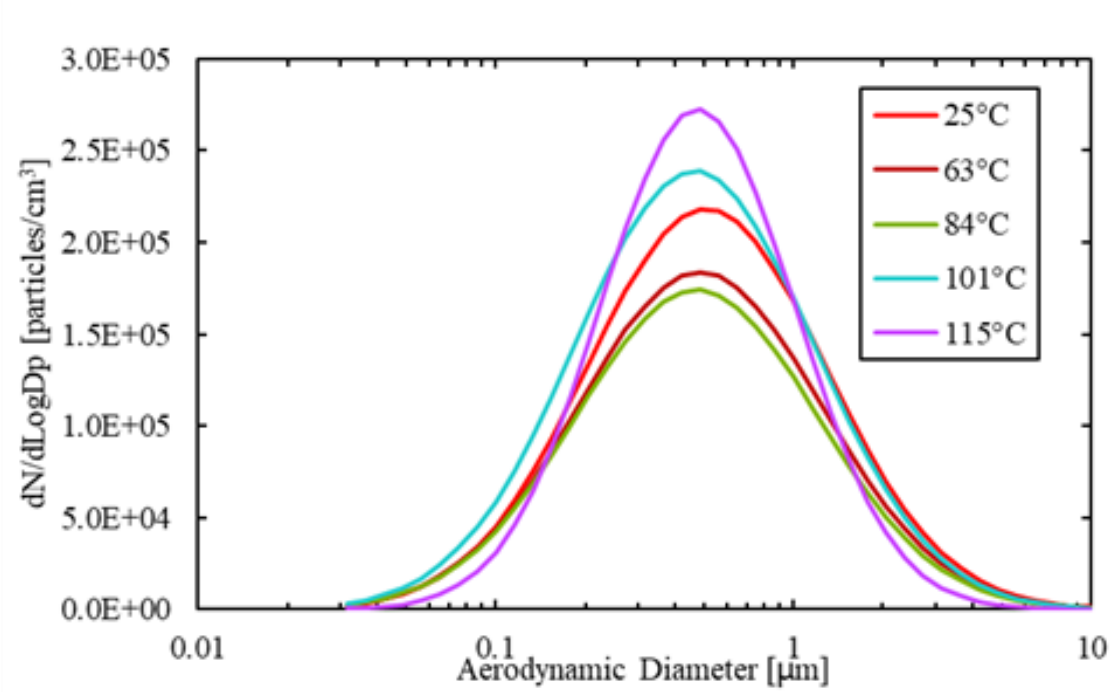


Figure 17: Log-normal fit for upstream number concentration as a function of temperature, standard 15W-40

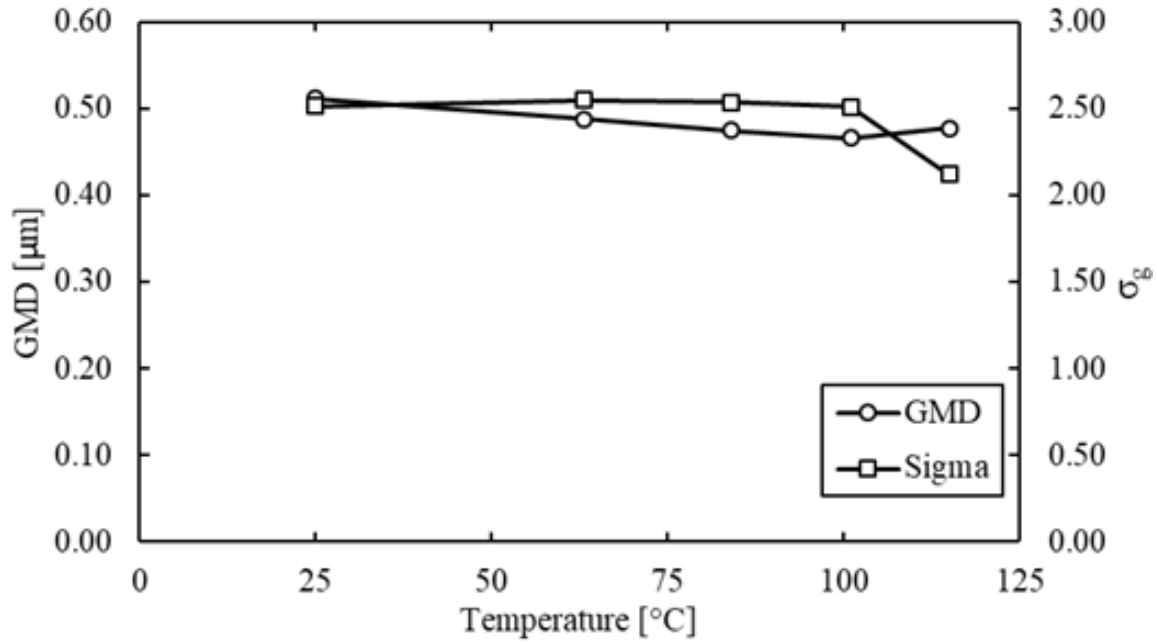


Figure 18: Upstream fit data for geometric mean diameter and $\sigma_g$ as a function of temperature, standard 15W-40

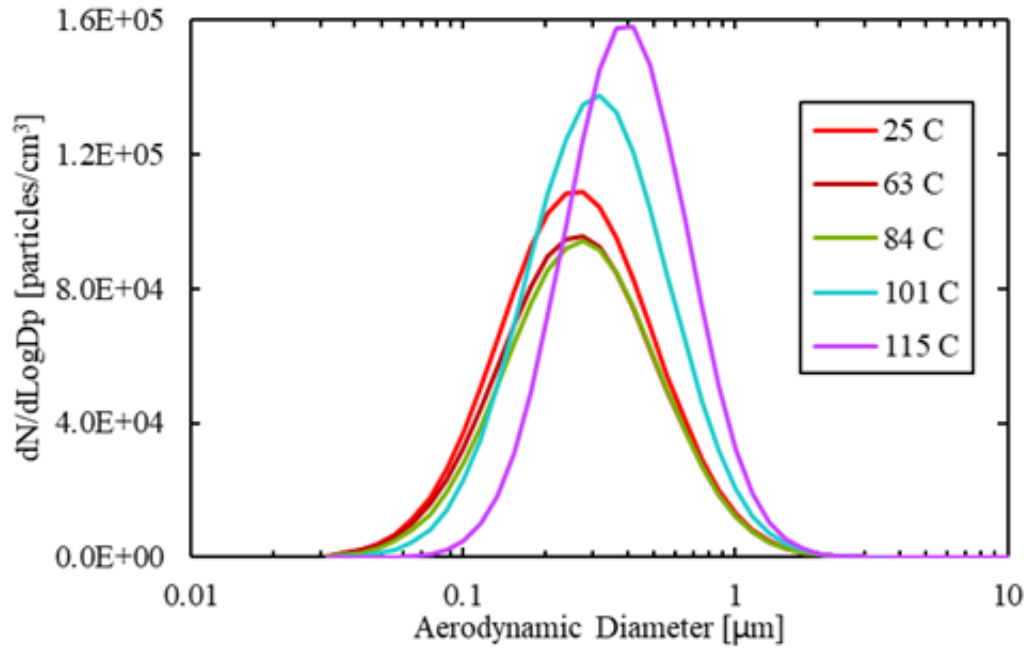


Figure 19: Log-normal fit for downstream number concentration as a function of temperature, standard 15W-40

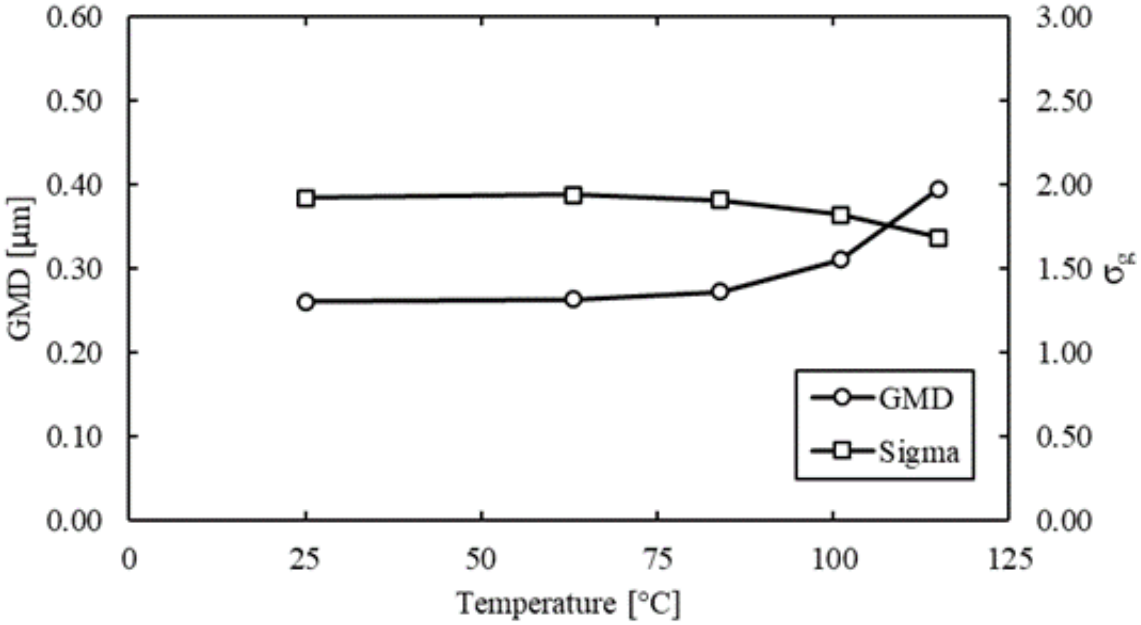


Figure 20: Downstream fit data for geometric mean diameter and $\sigma_g$ as a function of temperature, standard 15W-40

Figure 19 shows that as temperature increases, the width of the size distribution decreases, and the mean diameter increases as smaller particles disappear. These trends are summarized in figure 10, a plot of GMD and $\sigma_g$ against temperature. Figure 21 shows the number weighted and mass weighted size distributions downstream of the filter at room temperature. Comparing figure 21 with figure 15, reveals that the downstream particles are smaller on both a mass and number basis, and the downstream concentrations are substantially lower. Figure 22 is a plot of total mass and total number concentrations measured downstream against temperature. There is an initial decrease in concentration, then an increase for temperatures above 80°C.

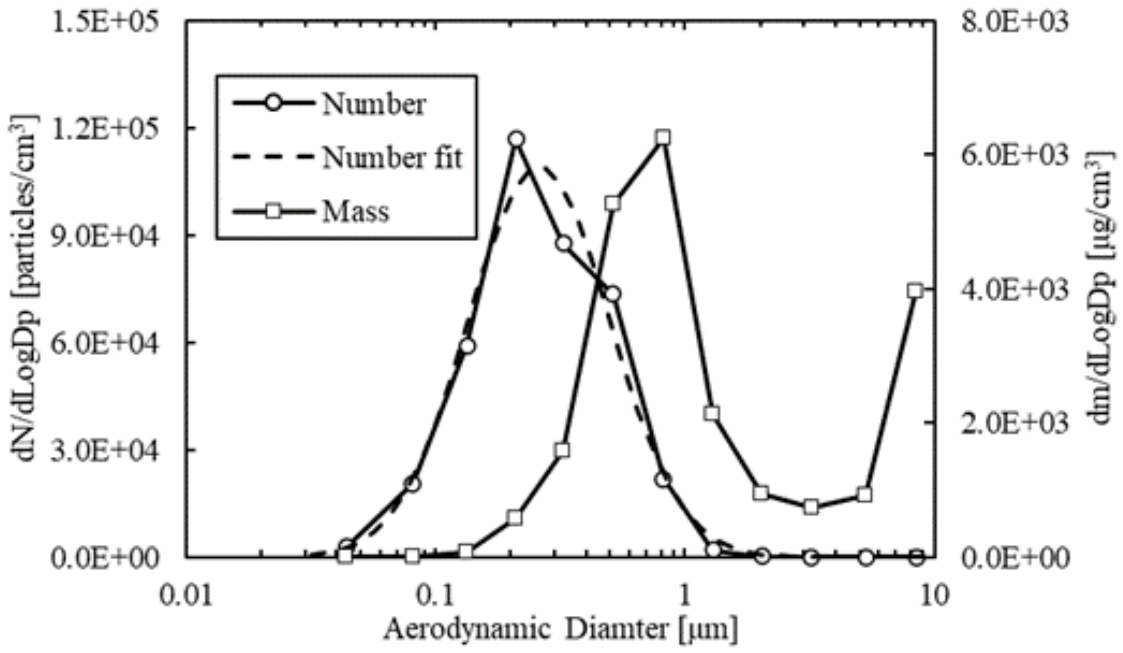


Figure 21: Mass, number and number fit downstream distribution for base case, 25°C

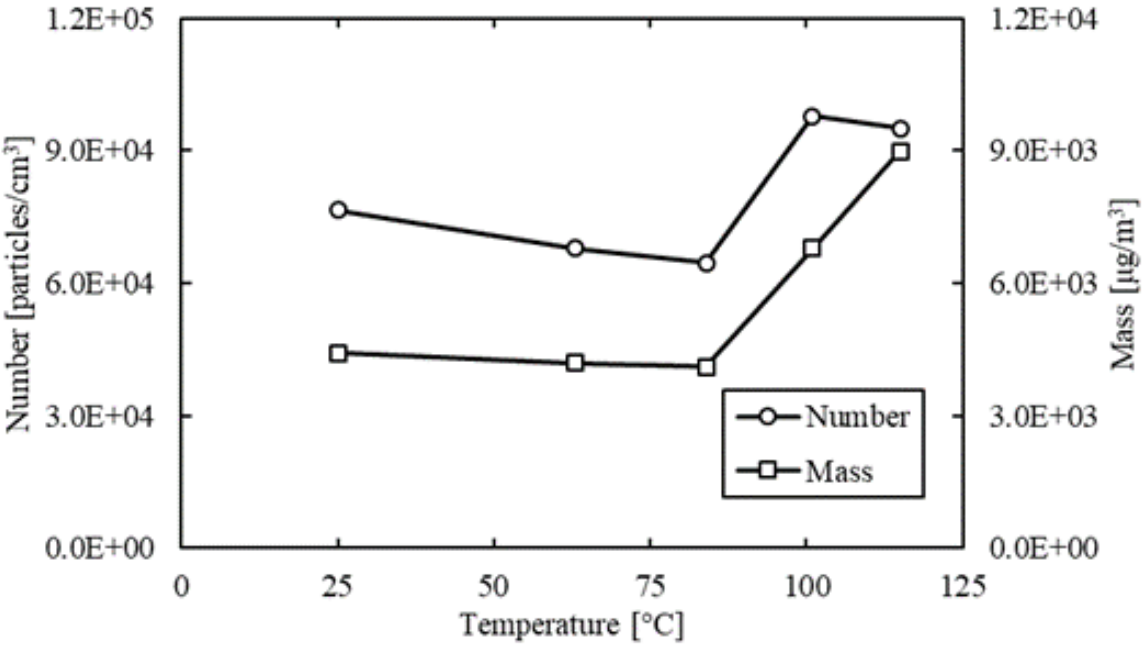


Figure 22: Total downstream mass and number concentration versus temperature

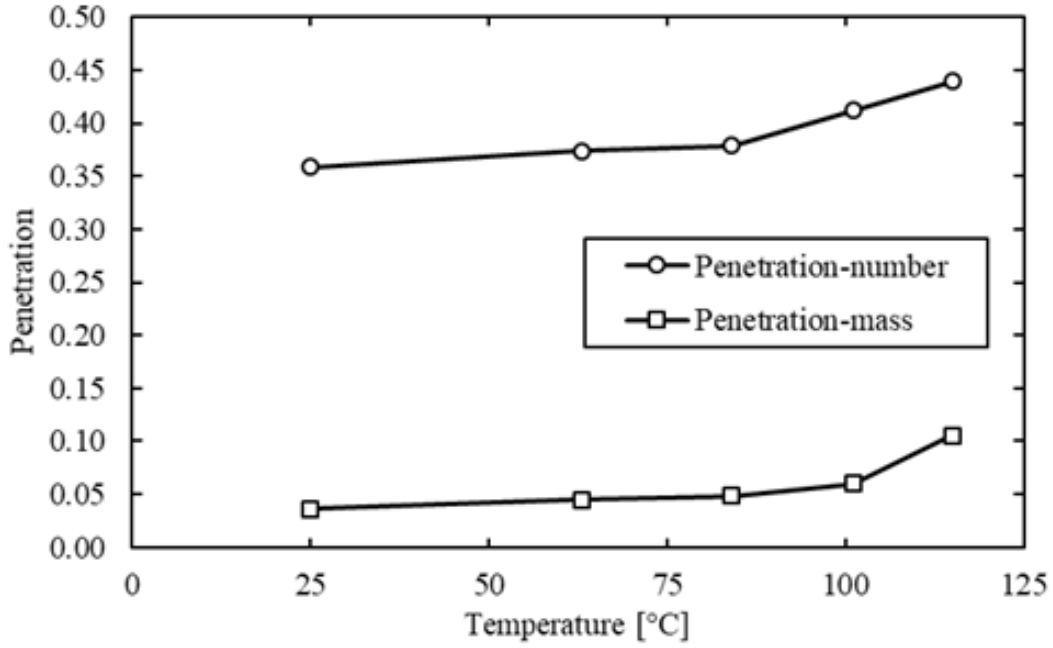


Figure 23: Coalescing filter mass and number weighted penetration as a function of temperature, standard 15W-40

The overall mass based, and number-based penetrations are calculated using equation 14 below.

$$P = C(T_x)_{downstream} / C(T_x)_{upstream} \quad (14)$$

Where $C(T_x)$ represents the number or mass concentration at a given temperature. These ratios are calculated using the data plotted in figures 16 and 22 and are plotted against temperature in figure 23. Both number and mass based overall penetrations increase with temperature. This trend, as discussed above, is not predicted by filtration theory.

## *2.7 Discussion of Evaporation Model*

The following hypothesis is proposed to explain this behavior. Particles generated by the atomizer shrink due to evaporation of their more volatile components during their passage through the heated section and up to entering the oven, so that the particles entering the filter are smaller than the particles generated by the atomizer measured at room temperature. The filtration efficiency plot shown in figure 13 shows that the MPPS predicted by theory, and the MPPS measured at room temperature is between 0.15 and 0.25μm. Figure 15 shows that most of the particle mass and number is contained in particles larger than this MPPS range so that if the particles shrink by evaporation in the heated section leading to the filter, they will be filtered less efficiently. Two things are necessary for this to occur: (1) the particles must contain a significant fraction of volatile components and (2) evaporation of these components must fast enough that significant shrinkage can take place during the 3 second residence time in the heated line. The discussion below makes a case that both conditions are likely to be met for common engine lubrication oils.

Cumulative mass fractions of alkanes (normal + branched + cyclo) adapted from Liang, et al. [18] are plotted against carbon number in figure 24. They only included carbon numbers up to C32 and about 30% of the mass fraction is expected in higher carbon number alkanes and constituents other than alkanes, e.g., aromatics. It is clear from figure 24 that more than half of the particle mass is contained in alkanes with carbon number C28 and below.

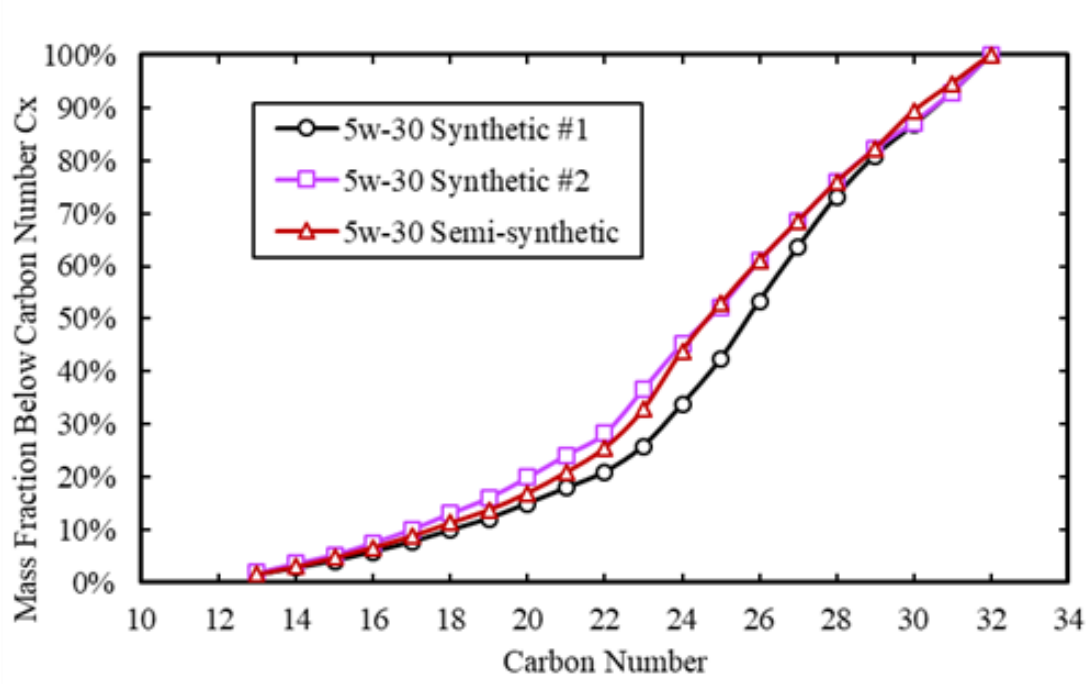


Figure 24: Cumulative mass of alkanes below $C_x$ plotted against carbon number for several modern lubricating oils, data from Liang, et al.

Tables 3 and 4 show the calculated evaporation times for C20, C24 and C28 normal alkane droplets of initial diameter, $d_p$=0.5μm and $d_p$=1.0μm. The expressions used for calculating particle evaporation and condensation rates are shown in section 2.5 above. These calculations are based on normal alkane vapor pressures from [19] and diffusion coefficients from [20]. For simplicity, it is assumed that the evaporation rates of all the alkanes of a given carbon number are the same and that evaporation takes place from

individual droplets of a given carbon number. The residence time in the heated section leading up to and including the filter is approximately 3 seconds. Thus, evaporation times of 3 s or less correspond to significant evaporation, but for the following discussion 1s is used as a conservative estimate. At 115°C, for 0.5μm particles, even for the highest carbon number, C28, the evaporation time is only 0.91s so sufficient time is available for evaporation most of the constituents up to C28, while for 1μm particles, by interpolation, the evaporation time of a C26 particle is 1s, thus sufficient time is available for evaporation of the constituents up to about C26.

Table 3: Evaporation time for normal alkane droplets C20, C24, C28 as a function of temperature, initial diameter, $d_p$=0.5μm

| | **Evaporation Time [s]** | | |
|---|---|---|---|
| **T [°C]** | **C20** | **C24** | **C28** |
| 25 | 53 | 1500 | 68000 |
| 70 | 0.25 | 5.4 | 120 |
| 80 | 0.09 | 1.9 | 37 |
| 90 | 0.03 | 0.68 | 12 |
| 100 | 0.014 | 0.26 | 4.1 |
| 110 | 0.006 | 0.11 | 1.5 |
| 115 | 0.004 | 0.07 | 0.91 |

Table 4: Evaporation time for normal alkane droplets C20, C24, C28 as a function of temperature, initial diameter, $d_p$=1.0μm

| | **Evaporation Time [s]** | | |
|---|---|---|---|
| **T [°C]** | **C20** | **C24** | **C28** |
| 25 | 210 | 6100 | 270000 |
| 70 | 1.0 | 21 | 480 |
| 80 | 0.36 | 7.4 | 150 |
| 90 | 0.14 | 2.7 | 47 |
| 100 | 0.06 | 1.0 | 16 |
| 110 | 0.02 | 0.42 | 5.9 |
| 115 | 0.02 | 0.27 | 3.7 |

As seen in figure 24, about 75% of the alkanes are below C28 and 55% below C26. But alkanes up to C32 constitute only about 70% of the particle mass so the corresponding fractions of oil droplet mass lost are 53 and 39%. Assuming spherical particles and constant density, these mass reduction factors correspond to a diameter reduction factors (1/0.47)1/3 = 1.29 and (1/.61)1/3 = 1.18 for 0.5 and 1.0 μm particles respectively. This decrease in diameter moves the particles toward the MPPS and consequently increases the penetration of particles through the filter, decreasing the overall filtration efficiency.

Referring to figures 16, 17 and 18, there is very little change in the upstream size distribution with temperature even though the aerosols are heated to temperatures as high as 115°C, and based on the calculations above, this would lead to significant shrinkage. Why doesn't it? During the entire heating, filtering, and sampling processes the particles are in intimate contact with their associated vapors. There is no dilution in the sampling

system, so evaporated vapors are not diluted, lost. We suggest that the evaporation and condensation create a dynamic balance between the particles and their associated vapors. Particles shrink in the heated section before the upstream sampling port but regrow as they cool passing through the upstream sampling line to the ELPI.

Tables 5, 6 and 7 below show the calculated particle growth rates when cooling from the filter test temperature to the measurement temperature, essentially ambient. It is assumed that inside the oven at the test temperature, there is a dynamic equilibrium between the particles and their vapors. Recall from above that at 115°C, 0.5 μm and 1.0 μm particles shrink by factors of approximately 1.29 and 1.18 to diameters of 0.39 and 0.85 μm, respectively. Thus, they would have to grow by 0.11 and 0.15 μm , respectively, to return to their original sizes. The tables show that growth rate decreases with increasing particle size and carbon number with a 1.0 μm C28 particle growing at the slowest growth rate at 115C of 0.17 μm/s. The residence time in the sampling lines and the inlet section of the ELPI is about 5s. Based on these calculations, even for the slowest growing particles there is more than sufficient time for them to regrow to their initial room temperature size. For lower temperature conditions, the particles will shrink less and, correspondingly, will need to grow less. It is assumed that as the droplets cool, the vapor pressures of the particle constituents drop quickly, while the partial pressures of the vapors remain near their initial high temperature values. This will lead to overestimating the growth rates during cooling. However, the fact that measured upstream size distributions show nearly no temperature dependence suggests that condensation growth rates are sufficient to restore the particles to near their initial room temperature size.

Table 5: Growth rate for normal alkane droplets, C20, C24, C28 as a function of temperature, initial diameter, $d_p$ =0.25μm

| | **Growth Rate [μm/s]** | | |
|---|---|---|---|
| **T [°C]** | **C20** | **C24** | **C28** |
| 90 | 17 | 0.87 | 0.05 |
| 100 | 43 | 2.3 | 0.15 |
| 110 | 104 | 5.9 | 0.42 |
| 115 | 160 | 9.2 | 0.69 |

Table 6: Growth rate for normal alkane droplets, C20, C24, C28 as a function of temperature, initial diameter, $d_p$ =0.5μm

| | **Growth Rate [μm/s]** | | |
|---|---|---|---|
| **T [°C]** | **C20** | **C24** | **C28** |
| 90 | 8.4 | 0.44 | 0.03 |
| 100 | 21. | 1.2 | 0.07 |
| 110 | 52 | 3.0 | 0.21 |
| 115 | 79 | 4.6 | 0.35 |

Table 7: Growth rate for normal alkane droplets, C20, C24, C28 as a function of temperature, initial diameter, $d_p$ =1.0μm

| | **Growth Rate [μm/s]** | | |
|---|---|---|---|
| **T [°C]** | **C20** | **C24** | **C28** |
| 90 | 4.2 | 0.22 | 0.012 |
| 100 | 11 | 0.58 | 0.04 |
| 110 | 26 | 1.5 | 0.11 |
| 115 | 40 | 2.3 | 0.17 |

Despite these arguments describing particle shrinkage and growth, it may not be immediately obvious why the measured MPPS shifts to greater diameter with increasing temperature as illustrated in figures 4, 13 and 14. Consider a simplified situation to help understand this experimental observation. Assume a filter has 100% removal efficiency except between 0.1µm and 0.2µm where removal efficiency is 0%. In accordance with filtration theory, we assume that the removal efficiency curve is independent of temperature. If an aerosol is passed through the filter at room temperature, the only particles measured downstream will be between 0.1 and 0.2µm, as expected. Now assume the filter is tested with a lube oil aerosol at 115°C. Based on a typical carbon number distribution, vapor pressure distribution, droplet evaporation theory, and heating time, we would expect the particles to lose 50% or more of their mass when heated to 115°C. For spherical droplets that would correspond to a diameter reduction of at least 1.26. For simplicity, we assume that all particles shrink by the same ratio. These particles now pass through the filter at 115°C and only particles with diameters, at filtration temperature, between 0.1 and 0.2µm will pass through. When these particles are sampled downstream, they cool to ambient temperature surrounded by the vapors that evaporated during the heating process. This causes them to grow by a factor that may, given sufficient time, approach the original shrinkage ratio, 1.26. Thus, the only particles measured downstream will be between 0.126 and 0.252µm, and the MPPS window will be shifted to the right as observed experimentally. This represents the fractional efficiency of the combination of the filter and the measurement system, but not of the filter itself.

Figures 13 and 14 suggest another question. As temperature is increased from ambient to 115°C the MPPS shifts from about 0.15 to 0.4µm, a shift of 0.25µm. The

upstream size distribution for this case has a count mean diameter of about 0.5µm so a diameter ratio of 1/1.26 would correspond to a diameter decrease of only about 0.1µm, significantly less than the MPPS shift. The assumptions about evaporation and growth made here are quite conservative and these shifts in MPPS suggest that actual diameter shifts are greater than predicted by the simplified modeling done here.

The final case to consider is the negative efficiency result for high volatility oil processed by the coalescing filter, shown in figures 7 and 8. This was only observed in the coalescing filter results and not with the inertial separator in figure 12. This suggests that the behavior is dependent on the presence or removal of particles with the coalescing filter. One theory that has been investigated by Raynor [21] and considered by Mullins [22], is the mechanism of bubble bursting in coalescing filters. The bubble bursting hypothesis is a re-entrainment mechanism wherein satellite droplets can be produced from oil-film bubbles forming and collapsing on the rear surface of a coalescing filter. Figure 25 below provides a visual of the mechanism. This theory acts as a best understanding of what is likely causing negative efficiency with the high volatility oil, coalescing filter results. Satellite droplets in a certain size range can be produced by favorable oil properties in the high-volatility oil mix. This may be enhanced by greater evaporation rates of bubble-limiting components in the high volatility oil or other oil properties such as surface tension, where the high volatility oil serves as an extreme, greatest surface tension case when compared to the other test oils. This is purely speculation and can be further investigated with suggested future testing outlined in 4.1.

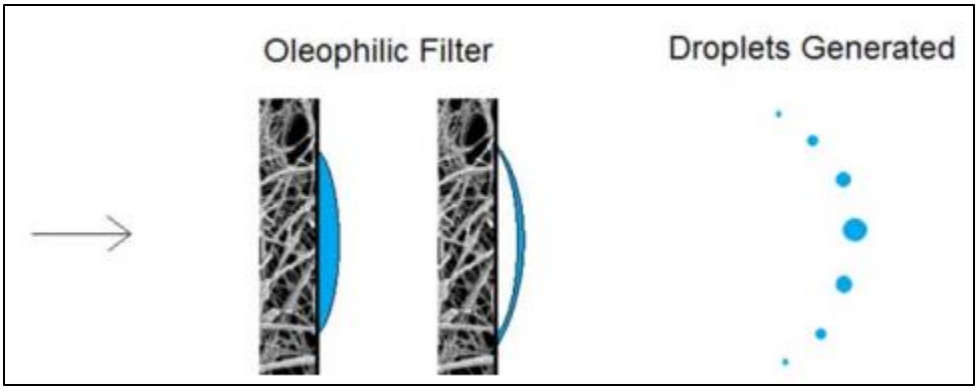


Figure 25: Droplet re-entrainment from the rear of the filter, illustrated proposed mechanism of satellite droplet formation, from Mullins et al. [22].

## *2.8 Chapter 2 Conclusions*

Two types of CV particle removal devices, a coalescing filter, and a rotating inertial device, were evaluated on a test bench designed to determine device fractional particle removal efficiencies. Tests were performed under isothermal conditions to a maximum temperature of 115°C, characteristic of what might be expected with an engine operating under high-load conditions. Four different lubricating oils were tested: a standard 15W-40 lube oil, a specially formulated high volatility engine oil, and two low volatility oils: a specially formulated low volatility engine oil, and synthetic vacuum pump oil. Particle size distributions and concentrations were measured in the size range from 0.043 to 8.46μm aerodynamic diameter using a Dekati Electrical Low-Pressure Impactor.

The measured oil particle removal efficiency decreased with increasing temperature and the MPPS shifted to larger diameters with the standard and high volatility oil. These shifts were observed with both the coalescing filter and the inertial device. Some shifts in the efficiency curves with temperature were also observed with the lower volatility oils, but the results were less consistent.

These observations support the hypothesis that multicomponent oil droplets lose their more volatile components and shrink by evaporation during heating. The geometric mean diameters of the oil droplets under test were in the range of 0.4-0.5μm by number and 1-2μm by mass at room temperature. This is larger than the MPPS of the devices tested, which is roughly between 0.15-0.30μm for the coalescing filter and between 0.08-0.12μm for the inertial device. Thus, particles initially larger than the MPPS shrink due to evaporation in the heated device, moving their size toward the MPPS, decreasing the overall filtration efficiency by both mass and number.

Particle evaporation calculations based on volatility of constituents of typical lubricating oils suggests that most of the lower carbon number components, below ~C26 to C28, will evaporate upon heating to 115°C. These lower carbon number components typically constitute 50% or more of the mass of a typical lubricating oil. A mass loss of 50% would lead to a decrease in spherical droplet diameter by a factor of $2^{1/3}$ or 1.26, thus shifting particles toward the MPPS as described above. Furthermore, experimental measurements made upstream of the filter showed that the upstream particle size distribution was essentially unchanged by heating over the entire temperature range investigated. This suggests that particles grow as the sample stream cools from test temperature to measurement temperature and evaporated vapors recondense. This supports the observation of the MPPS shifting to a larger diameter as test bench temperatures are increased and the cooling gradient to the sampling lines is increased.

Particle evaporation and condensation modeling suggests that there is sufficient time in the heated section leading to the device for loss of the more volatile components as indicated above and sufficient time for these species to recondense during sampling and

measurement. Thus, particles being measured are not the same size as the particles being processed by the removal device. Measurements made in this study reflect the performance of a CV system where heated droplets are processed by the device and surviving droplets grow as they cool downstream, and surrounding vapors condense, not the performance of the device itself.

# Chapter 3: Evaluation of Media and Low-Cost Gas Sensors for Indoor Air Quality Measurement

## *3.1 Introduction*

Indoor air quality has become an increasingly prevalent topic following the SARS-CoV-2 global pandemic. This is due to the transmission method of the virus: inhalation of airborne particles and droplets infected with the SARS CoV-2 virus [23]. Increased ventilation of indoor environments was recommended by the World Health Organization as the best virus abatement strategy. In addition to interest in improved ventilation, this led to the great demand for indoor air purification devices that could also be used for indoor pollutant control; consider the U.S. air purifier market size has grown from $1.8B to an estimated $2.5B from 2018 to 2021 with the majority of the market being commercial, followed by residential applications [24]. Demand also grew for devices that could be used for removal of both pollutant gases and particles including virus bearing particles. A considerable segment of the air purifier market is now also using activated carbon (activated charcoal) to go beyond particle removal, seeking to remove indoor pollutant gases not removed by traditional fibrous filter particle removal media, responding to consumer demand.

This study evaluated pollutant gas removal effectiveness of several carbon-impregnated media, using a set of low-cost gas sensors (LCGS) while at the same time evaluating the performance of the LCGSs for pollutant gases typically found in indoor environments. The LCGSs were tested for accuracy, detection limits, and response time. Testing was performed at the T.E Murphy Engine Research Lab using a purpose built

pollutant gas removal test bench. The results from this study will be applicable to implementing LCGSs in air purification devices for a reasonable cost.

### 3.1.1 Media for Indoor Air Quality Management

Carbon media, or activated carbon (AC), is known to have adsorption properties for separation and purification of many gases [25]. This is due to the great surface area and porous structure along with high surface reactivity. There are many known gas-phase applications, though other adsorbents such as zeolites, alumina, and silica gels are still favored due to their lower cost [26–28]. If manufacturing cost can be reduced for AC filters while maintaining favorable characteristics, the implementation to indoor air purifiers will be able to reach a greater number of commercial and residential settings.

Activated carbon is a collective name for porous carbons manufactured with varying techniques containing carbonaceous materials. The materials include many organic materials such as wood, nutshell, coal, and coconut shells [29]. Using thermochemical processes to convert waste materials into activated carbon has also been considered [29, 30] and could substantially reduce AC costs while also reducing waste disposal or landfill related costs. Another method of AC production, and notably $CO_2$ emission free, is methane pyrolysis [31]. This is primarily a process for producing clean hydrogen from methane or natural gas, though solid carbon is also a product.

### 3.1.2 Role of Low-Cost Sensors

A future opportunity in the realm of indoor air purifiers is the incorporation of cost-effective gas sensing using low-cost gas sensors. This would be for use as an indicator or even potentially as an active control sensing component. For this to be a viable option, the

LCGS should add little to the cost of the air purifier, measure gas concentrations with sufficient accuracy, and function in a range of indoor conditions. This project used a set of Alphasense B-series electrochemical sensors and one NDIR type sensor, which are often used in environmental monitoring applications. The B-series sensors have a small footprint of 32mm and 16.5mm in height. They are available for a broad range of gases and can be removed after expiration and replaced easily when paired with a quick-connect, low noise individual sensor board. The sensors selected for this study were for monitoring carbon monoxide, nitric oxide, sulfur dioxide, nitrogen dioxide, carbon dioxide, and a combination nitrogen dioxide and ozone sensor. The sensors have a 24-month warranty period that serves as an indicator for speculating lifetime and cost an average of $52 for a single retail purchase. Bulk quantity cost would likely be much lower.

## *3.2 Objectives*

There were two primary objectives for this project. The first was to determine the performance of a set of low-cost gas sensors suitable for measuring typical indoor air concentrations. The key performance metrics of the LCGS were gas concentration accuracy, detection limit, and response time. The second objective was to measure the gas removal effectiveness for three proprietary carbon-impregnated fibrous media. The pollutant gas removal effectiveness was also to be tested at varied humidity conditions. The results from this study provide useful information for determining viability of sensor and media incorporation with various indoor air purification systems.

## *3.3 Test Bench and Instrumentation*

The following section is a description of the instrumentation and devices used in the low-cost pollutant gas sensor and carbon media test apparatus, constructed for this project at the University of Minnesota, Murphy Engine Research Laboratory.

### 3.3.1 Pollutant Gas Removal Apparatus

Figure 26 below is an instrument diagram depicting each component with a reference number allotted in table 8. The reference number, component and manufacturer, usage in the test system, and parameters operated within, are described in Table 8 below.

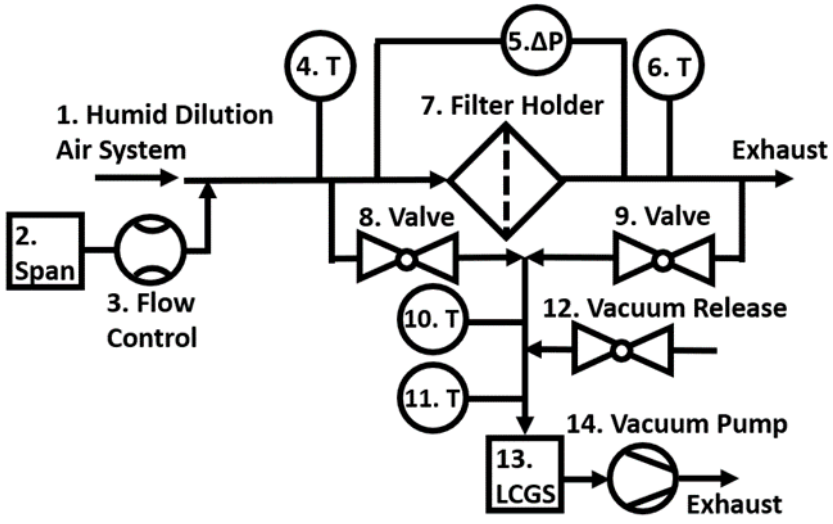


Figure 26: Pollutant gas removal apparatus for evaluation of low-cost gas sensor and panel media

Table 8: Instruments, manufacturers, and device parameters of operation

| Ref. # | Instrument<br>———<br>Manufacturer | Usage | Parameters of Operation |
|---|---|---|---|
| 1 | Humid Dilution Air System<br>———<br>In-house fabricated | Provides the clean, humidified dilution air to the test bench. | See 3.3.1 for description of system. |
| 2 | Span Gas Bottle + Regulator<br>———<br>Airgas calibration bottles. Various gases. | Provides the pollutant gas to the test bench. Diluted with Humid Dilution Air System at the inlet to the test bench. | Span bottle regulators are set to 40psi. |
| 3 | Span Flow Control System<br>———<br>Tube style LFE, needle valve, and Omega PX409-001DDU5V | Stainless steel tube style LFE throttled upstream with a needle valve. Omega differential pressure transmitter used with LFE characteristic equation to calculate flow. | Operated at 1-2 [L/min]. |
| 4, 6, 10 | Thermocouple<br>———<br>Omega K-type | Measuring flow temperature at sample point to ensure it is at target temperature. | Measuring system temperature. Near ambient temperature. |
| 5 | Differential Pressure Transmitter<br>———<br>Omega PX409-001DDU5V | Measuring the pressure drop across filter holder and or the equipped media. | Operated near 2 [inH2O] (0.07[psi]) |
| 7 | 8x10” Media Holder<br>———<br>Unknown Manufacturer | This is the panel media holder. The effective area was masked down such that a flowrate of 35 [LPM] resulted in a 5 [cm/s] media face velocity. | Operated at 5 [cm/s] face velocity for the majority of tests. |
| 8, 9 | Actuated valve<br>———<br>Unknown manufacturer | Actuator valves that are used to direct flow from upstream or downstream sample port. | Operated with 24 [V] source and controlled with NI 9472. |

| | | | |
|---|---|---|---|
| 11 | Humidity Sensor<br>———————<br>Omega HX71 | Used for monitoring sample humidity, which was assumed to be the same as test bench humidity. | Operated near 5%, lower limit, and near 60%. |
| 12 | Vacuum Release Valve<br>———————<br>Globe Valve | Used to release or prevent vacuum pressure in sampling line. Actuator valves , 8 and 9, are default closed. | Left open while the automated program was not running. This would allow for setup of sensing system without running the sampling program. |
| 13 | Low-Cost Gas Sensing Package<br>———————<br>Alphasense | See further detailed description of sensors and specifications in 3.2.2. | Operated at 0.5 [L/min]. |
| 14 | Vacuum Pump<br>———————<br>Unknown manufacturer | Used to pump a sample from the test apparatus and through the Low-Cost Gas Sensor Package | Operated such that sampling flowrate was 0.5 [L/min]. |
| - | DAQ Chassis and Modules<br>———————<br>NI cDAQ 9174<br>NI 9213<br>NI 9215<br>NI 9209<br>NI 9472 | 9174 is a compact DAQ chassis designed to operate up to four modules simultaneously through one USB connection. NI 9213 is a module for input and conversion of thermocouple signals.<br>NI 9215 is a module for collecting analog voltage signals, used here for logging pressure transmitter data.<br>NI 9209 is a module for collecting up to 32 single-ended voltage signals. Used for collecting EC sensor signals.<br>NI 9472 is a module for sourcing voltage output. This was used to control the sample line actuators. | Individual data points collected as an average of 100 samples captured at 100 [Hz], thus logging at 1[Hz]. |

### 3.3.2 Humid Dilution Air System

The Humid Dilution Air System was used to provide a flow of clean, humidity-controlled air to the pollutant gas removal apparatus. It is shown in figure 27. This is referred to by reference number 1 in Figure 26. The system is split in two halves seen in figure 27: the humid side, and the dry side. The first component to the humid side, is a cold bath ultrasonic humidifier which was operated with room air and distilled water. These

devices are known to generate significant concentrations of ultrafine particles, [32] aerosolizing dissolved solids present in the water. Even sub ppm impurity levels lead to significant particle generation. Downstream of the humidifier there is a droplet trap as well as a capsule HEPA filter. The droplet trap is a tube in tube counter-flow fixture that inertially and gravimetrically separates and drains larger incompletely evaporated water droplets. The capsule HEPA filter then removes smaller mainly solid residue particles generated by the humidifier as well as any particles present in the room air carrier gas. The last component in the humid side is a needle valve restricting total flow. The dry side for the system is simply the compressed air system supplied for the laboratory, with pressure reduced by a regulator and a needle valve. The laboratory compressed air is filtered and conditioned with a processing system that removes ambient $CO_2$ as well as water vapor. As shown in figure 27, the humid and dry sides converge then connect to the inlet of a piston type vacuum pump. The needle valves on the humid and dry sides were manually adjusted prior to starting a test to achieve the desired system humidity. The humidified air stream passes through the vacuum pump and then through another capsule HEPA filter to remove particles that may have been introduced by the pump. Finally, the flow passes through an Alicat flow controller which serves as a flowrate indicator rather than a controller. Instead, the flow is controlled via line restriction with the inlet needle valves on the humid and dry sides. The Humid Dilution Air System is connected to the pollutant gas removal apparatus as shown in figure 26.

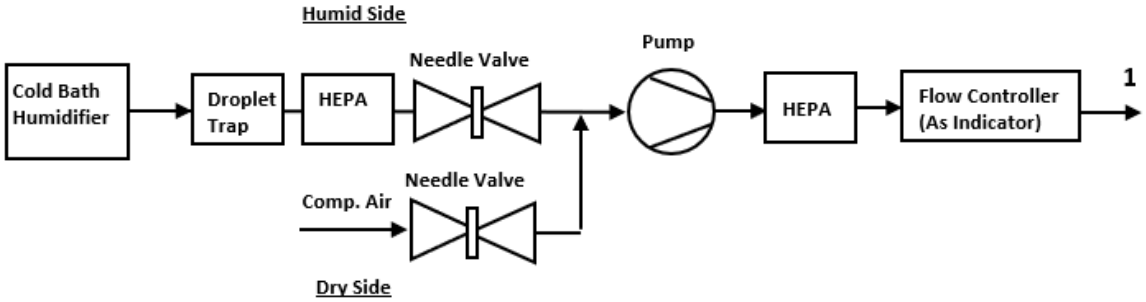


Figure 27: Humid Dilution Air System used in conjunction with the pollutant gas removal apparatus

### 3.3.3 Low-Cost Gas Sensor Package

The low-cost sensor package consists of a set of 6 AlphaSense pollutant gas sensors mounted in an aluminium plenum of approximately 0.15 L volume. The gas sensors included in the study were: carbon monoxide (CO), sulfur dioxide ($SO_2$), nitric oxide (NO), nitrogen dioxide ($NO_2$), combination ozone and nitrogen dioxide ($O_3$ + $NO_2$), and carbon dioxide ($CO_2$). Each of the sensor membrane faces are exposed to the inner sampling volume of the plenum and sealed from leakage with a gasket. When media testing, a sample was directed from either the upstream or downstream sample line to the plenum for concentration measurement. The same sensor package was used to measure both upstream and downstream concentrations separately.

Each of the sensors except for $CO_2$ (a NDIR sensor) are electrochemical (EC) type sensors. These electrochemical sensors have four electrodes: working electrode (We), reference electrode, counter electrode, and auxiliary electrode (Ae). Figure 28 below is a simplified illustration of a typical EC sensor. In brief, the working electrode is where oxidation or reduction of the pollutant gas occurs, the reference electrode connects

potentials to the working electrode for maintaining stable overall potential, the counter electrode balances the working electrode by reducing other molecules to produce opposite equivalent current, and the auxiliary electrode serves as a control version of the working electrode with the same characteristics and no contact with the pollutant gas.

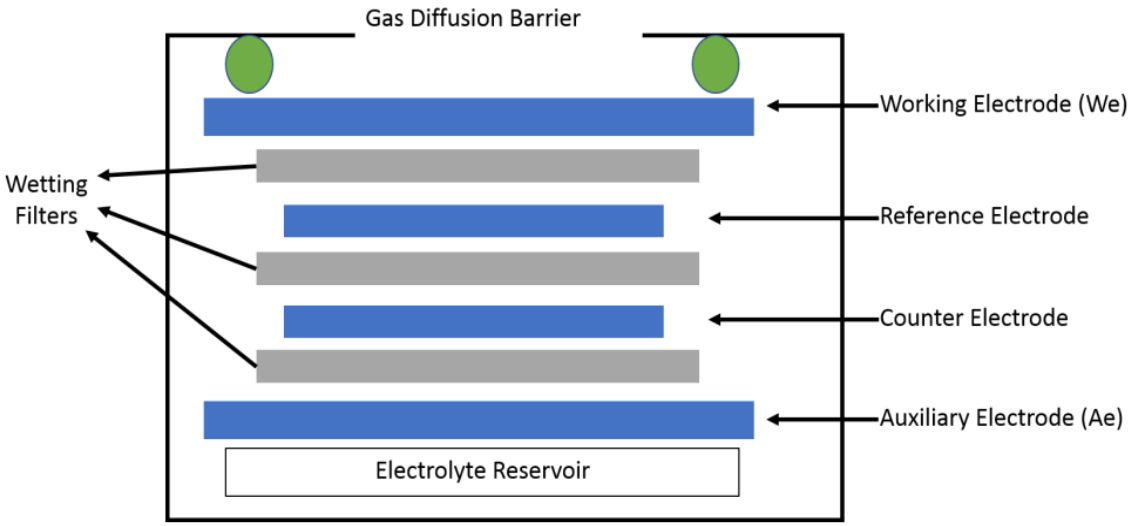


Figure 28: Electrochemical sensor sectional view from AlphaSense [33]

Table 9 below gives the main specifications of the sensor package obtained from Alphasense. Specifications are listed for each of the sensors except for the combination ozone and nitrogen dioxide sensor OX-B431. The specifications for this sensor are the same as the nitrogen dioxide sensor, the only difference being an ozone filter is present on the $NO_2$ only sensor.

Table 9: Electrochemical Sensors and Specifications from Alphasense [34]–[38]

| Pollutant Gas | **NO** | **CO** | **$SO_2$** | **$NO_2$** | **$CO_2$** |
|---|---|---|---|---|---|
| Sensor Range | 20 ppm | 1000 ppm | 100 ppm | 20 ppm | 5000 ppm |
| Sensor Noise (Manufacturer) | 15 ppb | 4 ppb | 5 ppb | 12 ppb | 50 ppm |
| Response Time [s] | 45 | 30 | 60 | 25 | 40 |
| Product Title | NO-B4 | CO-B4 | SO2-B4 | NO2-B43F | IRC-A1 |

## *3.4 Procedures*

### 3.4.1 Operating Procedures

The steps listed below were followed for each test with the pollutant gas removal apparatus. This was in effort to minimize uncertainty associated with operator error. The steps (1-7) are described briefly below.

1. Select Media

    i: Insert media being tested into 8x10 inch panel media holder

2. Turn on vacuum pumps

    i. Pump for pulling flow through test bench

    ii. Pump for Humid Dilution Air System

3. Adjust Humid Dilution Air System to target flow

    i. Open dry and humid side valves

    ii. Adjust humid to dry valves to achieve desired relative humidity

4. Span Flow Control System opened and set to target flow

    i. Span gas bottle opened

ii. Needle valve adjusted to meet target flow of span

5. Vacuum release valve closed, and program started

i. Launch LabView software program on laptop

ii. Close the vacuum release valve

iii. Start the LabView program

iv: Ensure LabView pre-set configuration for sample switching period is 120s

6. Operating

i. Test bench LabView control continues switching between upstream and downstream sampling streams until the program is stopped

7. Finishing Operation

i. End program after target run time has elapsed, often 30min

ii. Close all flow controlling valves, open vacuum release valve, power down all other equipment

### 3.4.2 Calibration

Two parts of the apparatus required calibration. The first was determination of the dilution of the span flow for the Humid Dilution Air System used to calculate diluted span gas concentration, and the second was calibration of the sensors using diluted span gas and the regression method of sensor calibration.

A tracer gas was used to determine the span gas flow dilution ratio when operated with the Humid Dilution Air System, which is further described in section 3.2.1. Although the dilution ratio could have been determined from measured flows of span gas and humid air, the tracer method could be implemented without major revisions to the test bench and

decreased system uncertainty. The tracer gas of choice was $CO_2$, which was chosen for safety and because it could be measured with a high accuracy $CO_2$ gas analyzer. The gas analyzer used was a Sable Systems CA-10 Carbon Dioxide Analyzer. It was operated in place of the Low-Cost Gas Sensor Package for a set of different dilution ratio conditions. The flow of dilution air was measured using a Sensidyne Gilibrator 2 and the flow of span could then be calculated using the measured $CO_2$ concentrations with the CA-10 of a known $CO_2$ span. Correction factors were calculated for correcting the indicated flow of each the dilution and span lines, each being near 1%, and embedded in the LabView operating program.

Alphasense electrochemical sensor calibration data were fit to a linear regression model. The regression model is shown below in equation 15.

$$Concentration = \beta_0 + (\beta_1 \cdot We) + (\beta_2 \cdot Ae) + (\beta_3 \cdot T) + (\beta_4 \cdot R.H.) \quad (15)$$

In equation 15, *Concentration* is the known pollutant gas concentration calculated using the known concentration from the span supply and the dilution ratio from the Humid Dilution Air System. Here, *We* is the working electrode output signal in volts, *Ae* is the auxiliary electrode output in volts, *T* is the sensor temperature, and *R.H.* is the relative humidity at the sensor face. Each of these four signals were captured with their respective sensors; temperature was captured with a thermocouple mounted in the sampling line, relative humidity was measured with an Omega humidity sensor in the sampling line, and the *We* and *Ae* signals were captured as analog signals from the gas sensor of interest. The beta coefficients are regression coefficients for each of the respective inputs, along with an intercept term $\beta_0$. The coefficient $\beta_1$ is for the working electrode, $\beta_2$ is for the auxiliary electrode, $\beta_3$ is for the temperature, and $\beta_4$ is for the relative humidity.

As seen above, the sensor response depends on gas concentration, relative humidity, and temperature. For these calibrations, the gas concentration and relative humidity were directly controlled independent variables. The sensor response also depends on temperature, and in this case the temperature was not directly controlled, but rather recorded as an independent variable. For each media test, calibrations were performed immediately after each media test. This was done to ensure that the calibrations were appropriate to the range of test conditions observed. Typically, calibrations used 20-25 randomized set points.

### 3.4.3 Data Analysis Techniques

As mentioned in sections 3.3 and 3.4.1, the same set of low-cost gas sensors were used to measure gas concentrations for the upstream and downstream gas flow paths. Switching between sampling ports had to occur often enough that media performance changes with time could be captured, while still allowing enough time to accurately measure gas concentrations. The approach used was to allow sufficient time for the current sample to flow through the entire sample line then mix in the LCGS plenum until gas concentrations were steady. Tests done with the $CO_2$ tracer gas showed that this stabilization time was 30-40s. These tests are described in more detail in section 3.5. This portion of the sampling, stabilization time, was rounded up to a standard 60s. After stabilization, data were captured for 60s. Thus, each upstream or downstream data collection window lasted 120s, 60s stabilization followed by 60s measurement.

To process the data, a program was written to omit the first 60s of every 120s sampling period. The raw sensor data signals were also processed into 10s running averages to smooth the sensor signals. The running average had to be implemented because

sensor noise effects of each sensor were causing poor concentration calculations with the regression equation coefficients which were calculated using averaged data point collections.

## *3.5 Results and Discussion*

Table 10 is a test matrix showing a sequential listing of the tests, humidity, and calibration conditions. The calibration dates are listed on the same date as testing or after for each of the gases. In cases where they were performed on the same day, the calibration was performed immediately after testing to acquire accurate regression coefficients. The other advantage to performing calibration after media testing was the ability to target gas concentrations observed on the downstream side. This was done by referencing the raw sensor signal output voltage, *We*, range during media testing and ensuring that the same range was encompassed during calibration.

Table 10: Sequence of Testing Media and Sensor Calibration with Various Gases

| Month/Day/Year Tested | Calibration Date | Calibration Concentration Range | Pollutant Gas Test | Dry or Humid |
|---|---|---|---|---|
| *November 2021* | - | - | - | - |
| 11/15/2021 | 11/18/2021 | 0→3000 ppm | $CO_2$ | Dry |
| *May 2022* | - | - | - | - |
| 05/17/2022 | 05/17/2022 | 0→0.11 ppm | $NO_2$ and $NO_2/O_3$ | Dry |
| 05/27/2022 | 05/27/2022 | 0→0.91 ppm | NO | Dry |
| *June 2022* | - | - | - | - |
| 06/02/2022 | 06/02/2022 | 0→24 ppm | CO | Dry |
| 06/02/2022 | 06/02/2022 | 0→4.8 ppm | $SO_2$ | Dry |
| *July 2022* | - | - | - | - |
| 07/19/2022 | 07/19/2022 | 0→802 ppm | $CO_2$ | Humid |
| 07/19/2022 | 07/19/2022 | 0→9.14 ppm | CO | Humid |
| 07/19/2022 | 07/19/2022 | 0→4.0 ppm | $SO_2$ | Humid |
| 07/19/2022 | 07/19/2022 | 0→0.4 ppm | NO | Humid |
| 07/26/2022 | 07/26/2022 | 0→0.44 ppm | $NO_2$ and $NO_2/O_3$ | Humid |

First, calibration of the sensors will be demonstrated. This is followed by results of each media test shown in plots of gas concentrations measured upstream and downstream of the media against time. For each gas and media, the results of tests made under humid and dry conditions are plotted side by side. Gas removal efficiencies are not plotted because for most gas / media combinations efficiencies are low. Instead, efficiency results are presented in section 3.5.7, table 14. Some of the results of testing media C have been omitted due to operator error during testing.

### 3.5.1 Sensor Calibration

Calibration procedures were performed the same for each sensor as described in 3.4.2. The calibration results for the $NO_2/O_3$ combination sensor are shown in figures 29 and 30 below. These figures represent the typical response during final 60s of 120 s test exhibited by each of the EC sensors during calibration.

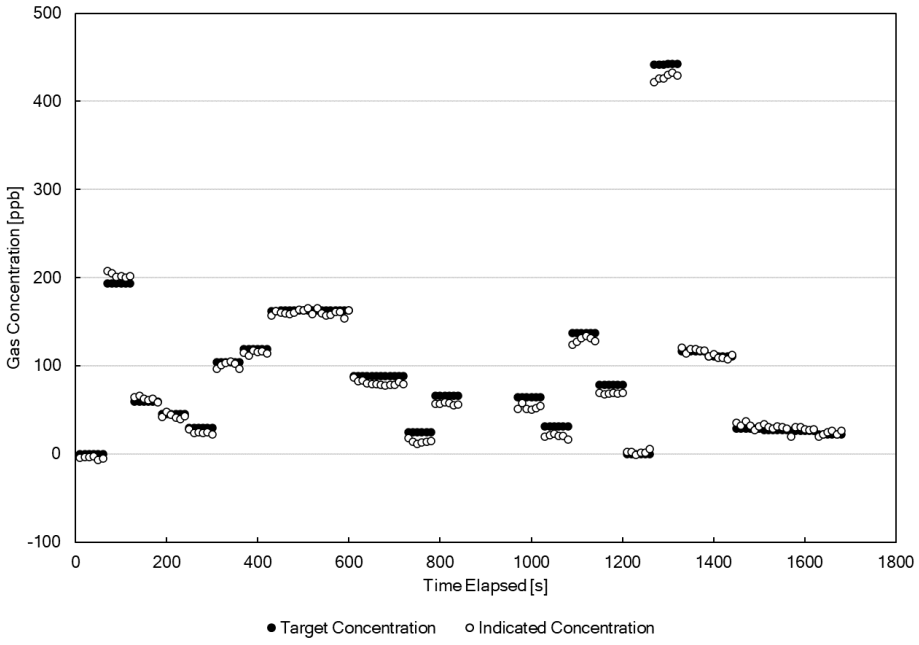


Figure 29: Target gas concentrations versus indicated sensor response after regression calculation, $NO_2$ / $O_3$ combination sensor

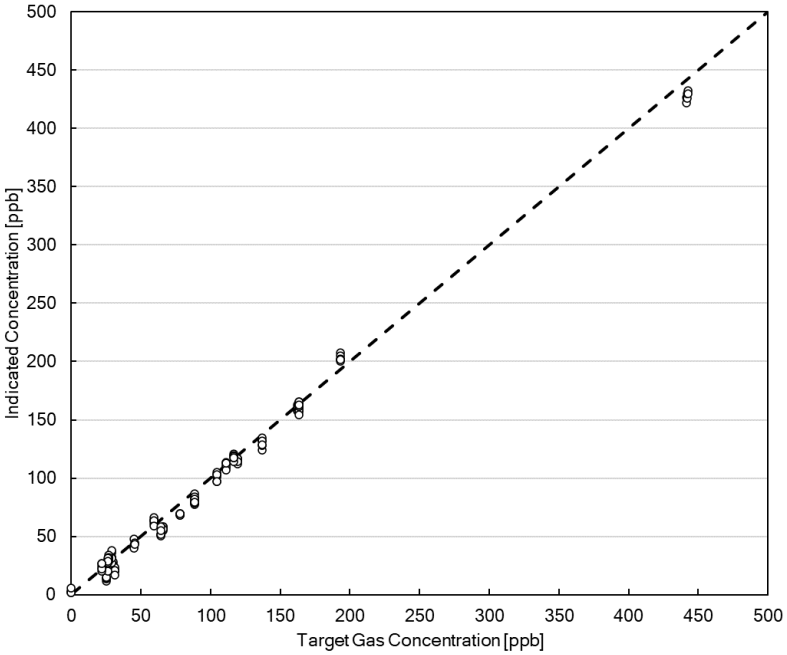


Figure 30: Calibration curve for indicated concentration versus target gas concentration, $NO_2$ / $O_3$ combination sensor

Figures 29 and 30 contain the same data set presented in two different orientations. In figure 29, the calibration set is shown in chronological sequence with data filtering included. The data filtering was simply to remove the 60s of stabilization between set points. Randomized dilution points and measurement periods between each set point were manually controlled with a minimum of 120s periods including stabilization. This was a typical calibration regime and sensor response, exhibited similarly by each of the EC sensors. Figure 30 has the data plotted to a calibration curve to indicate the sensor agreement with set points. The calibration figures demonstrate that calibration and the application of regression coefficients for was performed correctly. The $r^2$ values for indicated versus target concentration serve as an indicator for accurate calibration. The $r^2$ values are as follows: $r^2_{CO}$=0.984, $r^2_{CO2}$=0.977, $r^2_{SO2}$=0.968, $r^2_{NO}$=0.995, $r^2_{NO2}$=0.996,

$r^2_{NO2/O3}$=0.994. The lesser of two $r^2$ values was used for each sensor since each was calibrated for both humid and dry conditions.

Noise of the gas sensors was interpreted using calibration data. Noise was interpreted as the standard deviation of the sample at a zero point. The noise observed has also been smoothed during data capture where the DAQ, described in section 3.3, averaged 100 raw data points into a single captured data point at 1Hz frequency. Results are tabulated in Table 11 with the manufacturer specification included.

Table 11: Low-Cost Gas Sensor Noise

| Pollutant Gas | **NO** | **CO** | **$SO_2$** | **$NO_2$** | **$NO_2/O_3$** | **$CO_2$** |
|---|---|---|---|---|---|---|
| Noise Observed | 3 ppb | 31 ppb | 83 ppb | 3 ppb | 2 ppb | 2 ppm |
| Sensor Noise (Manufacturer) | 15 ppb | 4 ppb | 5 ppb | 12 ppb | 12 ppb | 50 ppm |

The observed noise was higher than specification value for two of the gas sensors, CO and $SO_2$. Observed noise was lower for the remaining 4 sensors which were NO, $NO_2$, $NO_2/O_3$, and $CO_2$. The greatest deviation from manufacturer specification was the NDIR type CO2 sensor, where 2ppm of noise was observed compared to the specification value of 50ppm.

Response time was another key metric was for each gas sensor that could be interpreted from the calibration data. This was calculated as the time from 10% to 90% change in indicated concentration in response to a step change in span gas concentration. Time constant values were all calculated between two non-zero concentration setpoint values. Figure 31 shows typical EC sensor response to a step change in gas concentration.

It should be noted that the sensor signal could not be displayed as an indicated gas concentration in figure 31 at 1hz frequency because of the running average required for the regression coefficients to produce meaningful results. This was due to the combined noise in the four sensor signals used to calculate indicated concentration, which produces meaningless results when interpreted on 1hz scale. Instead, the raw sensor output, *We*, is shown along with the initial and final indicated concentrations.

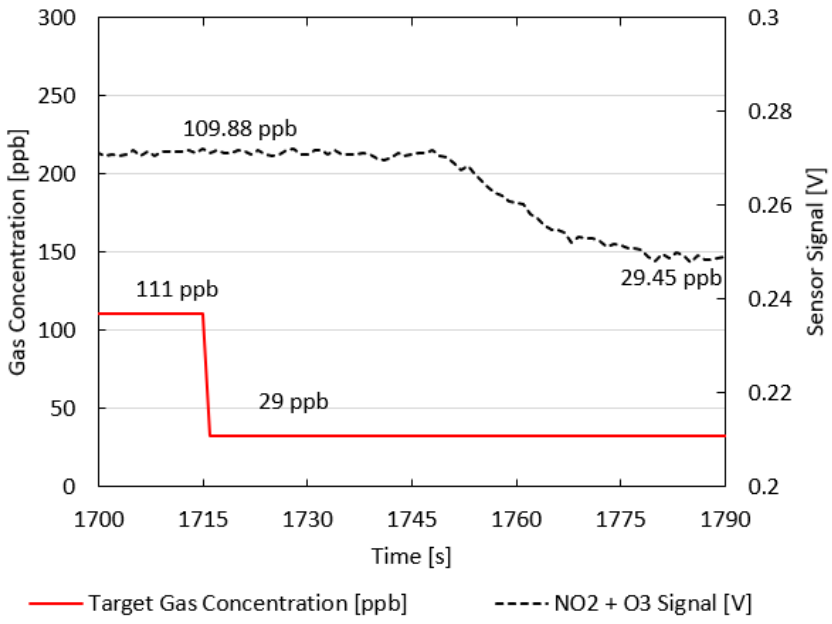


Figure 31: Signal Response to Gas Concentration Step, $NO_2$ and $NO_2/O_3$ Sensors

There is a clear lag between the drop in gas concentration and the first change in sensor response. This is due to the residence time of the system. System residence time was calculated as shown in equation 16.

$$Residence\ Time = t_{test\ bench} + t_{sampling\ line} + t_{plenum} \tag{16}$$

Where $t_{test\ bench}$ is the time to transport from the system inlet to the upstream sample port, $t_{sampling\ line}$ is the transport time in the stainless steel sampling lines, and $t_{plenum}$ is the effective time for the entire LCGS plenum volume to exchange with sampled gas. $t_{test\ bench}$ was calculated using the system flowrate, length and piping diameter and found to be approximately 2s. $t_{sampling\ line}$ was calculated with sampling flowrate, tubing length, and tube diameter, and was found to be approximately 11s. $t_{plenum}$ was calculated approximately as the plug flow through the plenum. Plug flow through the plenum was determined to be 18s. Note that the sample exchange in the LCGS plenum is not perfect due to mixing, though it could not be calculated as a well mixed scenario due to the laminar flow. Summation of the three times results in a system residence time of approximately 31s. Referring to figure 31, we see that the delay in response from the initial change in gas concentration is in reasonable agreement, where the initial change in gas concentration was at 1715s and the sensor had a first response near 1746s. The 10-90% response time of each sensor was determined from experiments like this. Table 12 displays the quantitative 10-90% response time results.

Table 12: Low-Cost Gas Sensor 10-90% Response Time

| Pollutant Gas | **NO** | **CO** | **$SO_2$** | **$NO_2$** | **$NO_2/O_3$** | **$CO_2$** |
|---|---|---|---|---|---|---|
| Response Time [s] | 14 | 42 | 41 | 26 | 26 | 64 |
| Response Time [s] (Manufacturer) | 45 | 30 | 60 | 25 | 25 | 40 |

From table 12 we see 4 sensors are near or faster than specification for response time. The CO and $CO_2$ sensors both responded slower than manufacturer specified. Note,

it was observed that sensor response times starting from non-zero values were notably faster than from zero starting values for equal change in magnitude. This was a qualitative observation and was not quantitatively investigated.

### 3.5.2 Media Testing Results for Nitric Oxide (NO)

Figures 32, 33, and 34 show results for media A, B, and C, respectively. Expected upstream concentration of Nitric Oxide (NO) was 0.35 ppm for humid tests (60% R.H.) and 0.25 ppm for dry tests (5% R.H.). These plots, along with the additional plots shown for the other gases, will be discussed in detail below.

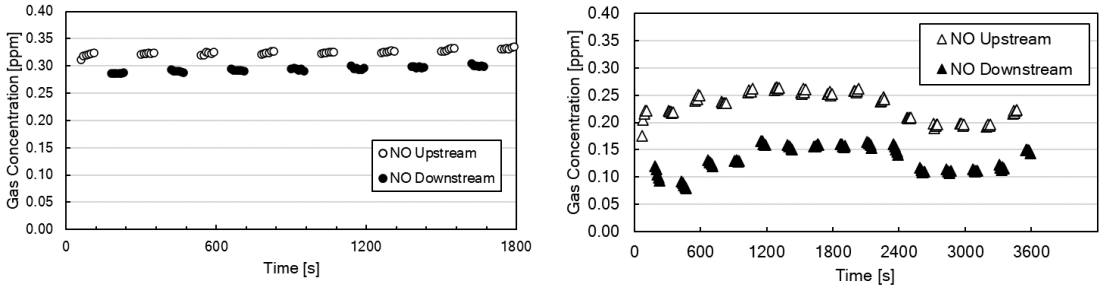


(a) (b)

Figure 32: Gas concentration versus time, NO, media A, (a) 60% R.H. (b) 5% R.H.

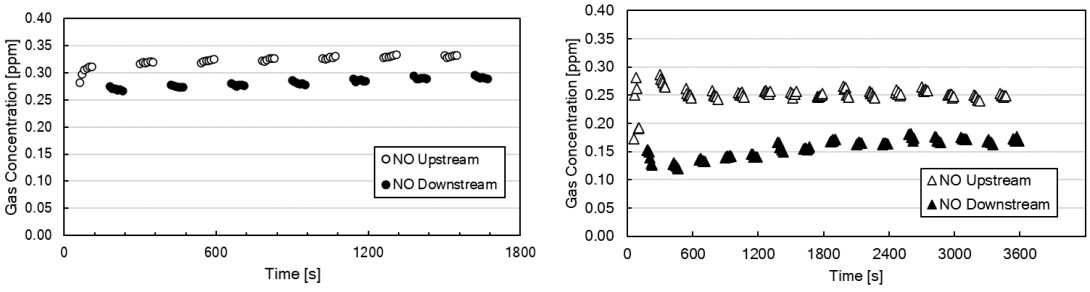


(a) (b)

Figure 33: Gas concentration versus time, NO, media B, (a) 60% R.H. (b) 5% R.H.

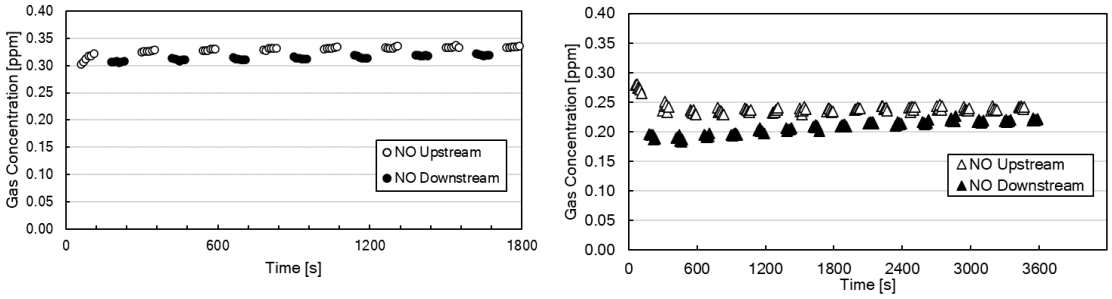


(a) (b)

Figure 34: Gas concentration versus time, NO, media C, (a) 60% R.H. (b) 5% R.H.

### 3.5.3 Media Testing Results for Carbon Monoxide (CO)

Figures 35, 36, and 37 show results for media A, B, and C, respectively. Expected upstream concentration of carbon monoxide (CO) was 6.5 ppm for humid tests and 20 ppm for dry tests.

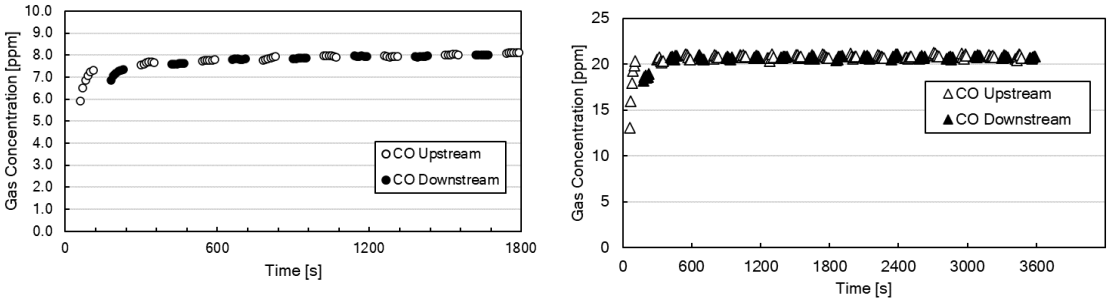


(a) (b)

Figure 35: Gas concentration versus time, CO, media A, (a) 60% R.H. (b) 5% R.H.

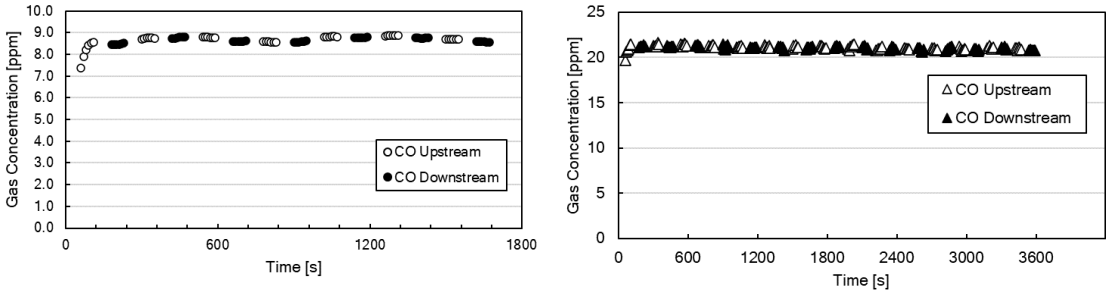


(a) (b)

Figure 36: Gas concentration versus time, CO, media B, (a) 60% R.H. (b) 5% R.H.

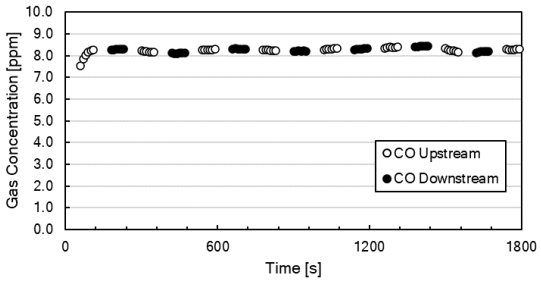


Figure 37: Gas concentration versus time, CO, media C, 60% R.H.

### 3.5.4 Media Testing Results for Sulfur Dioxide ($SO_2$)

Figures 38, 39, and 40 show results for media A, B, and C, respectively. Expected upstream concentration of sulfur dioxide ($SO_2$) was 1.5 ppm for humid tests and 4.0 ppm for dry tests.

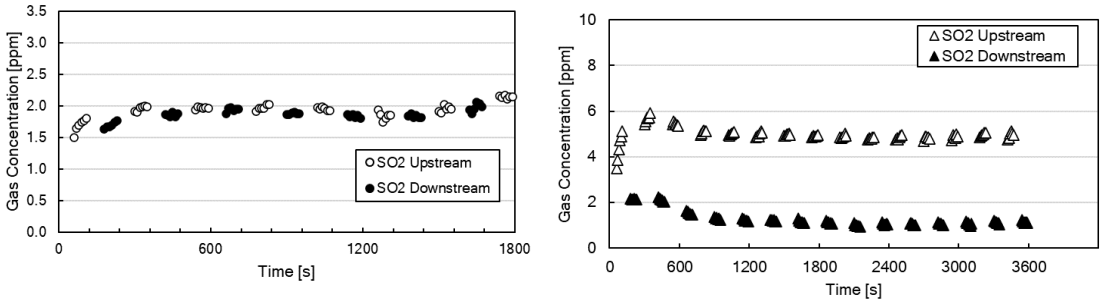


(a) (b)

Figure 38: Gas concentration versus time, $SO_2$, media A, (a) 60% R.H. (b) 5% R.H.

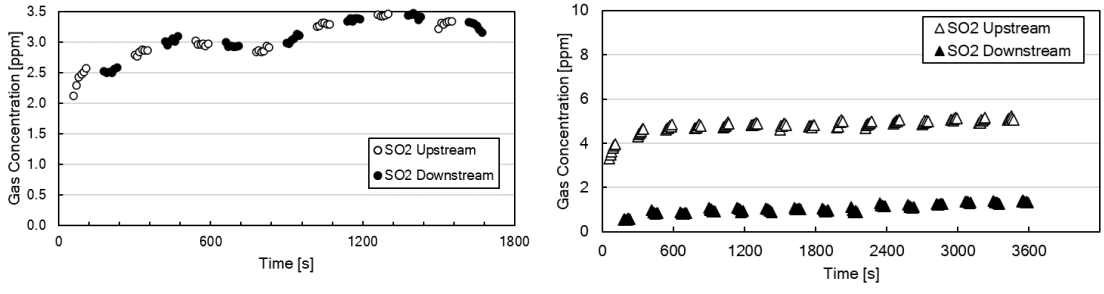


(a) (b)

Figure 39: Gas concentration versus time, $SO_2$, media B, (a) 60% R.H. (b) 5% R.H.

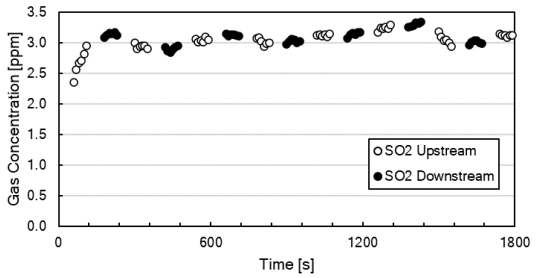


Figure 40: Gas concentration versus time, $SO_2$, media A, 60% R.H.

### 3.5.5 Media Testing Results for Nitrogen Dioxide ($NO_2$) and Combination $NO_2$, Ozone ($O_3$) Sensors

Unexpectedly large temperature variations were encountered during dry air media testing for nitrogen dioxide ($NO_2$) leading to large uncertainty. Temperature variation during the test day led to temperatures far outside the range used during calibration, ranging from 19 to 24°C, compared to the calibration temperature of 22.9±0.2°C. This variation was likely due to the building receiving door being left open to the outside environment. The temperature coefficient determined during calibration had a poor correlation and produced errors in the determination of gas concentrations. Consequently, only humid condition test data are shown below for the two $NO_2$ sensors. Figure 38 and 39 show concentrations for the two $NO_2$ sensors. Here, instead of showing humid and dry conditions, the left-hand plot refers to the $NO_2$ only sensor, and the right-hand plot to the combined $NO_2/O_3$ sensor. The expected upstream $NO_2$ concentration was 350ppb. Observed concentrations were much lower and further discussed in section 3.5.7.

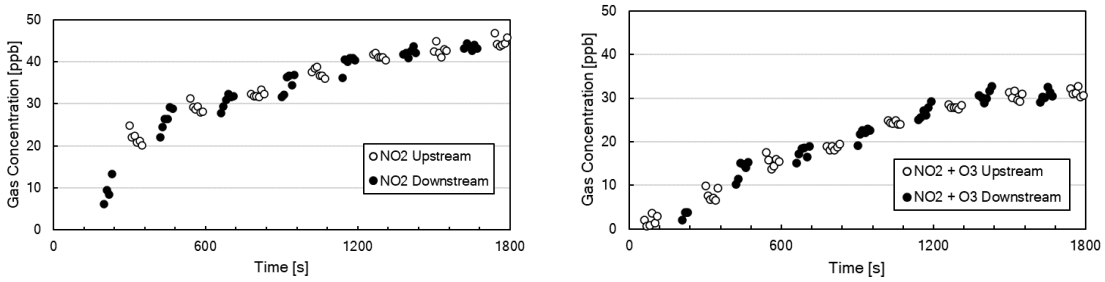


(a) (b)

Figure 41: Gas concentration versus time, $NO_2$, media A, 60% R.H. (a) $NO_2$ only sensor (b) $NO_2/O_3$ combined sensor.

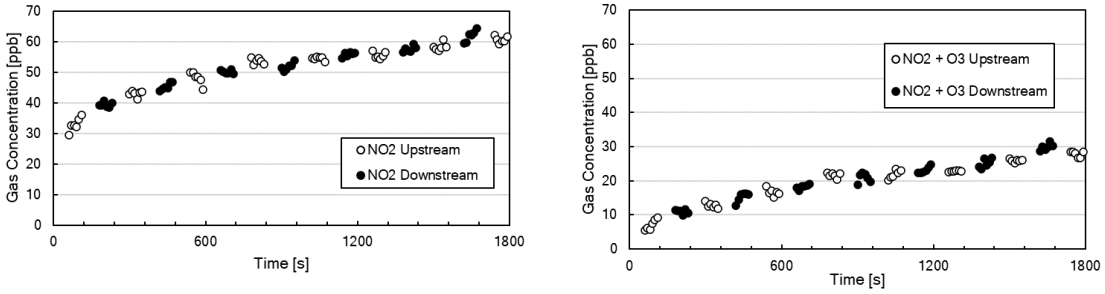


(a) (b)

Figure 42: Gas concentration versus time, $NO_2$, media B, (a) $NO_2$ only sensor (b) $NO_2/O_3$ combined sensor.

### 3.5.6 Media Testing Results for Carbon Dioxide

Figures 43, 44, and 45 show results for media A, B, and C, respectively. Expected upstream concentration for carbon dioxide ($CO_2$) was 400 ppm for humid tests and 3500 ppm for dry tests.

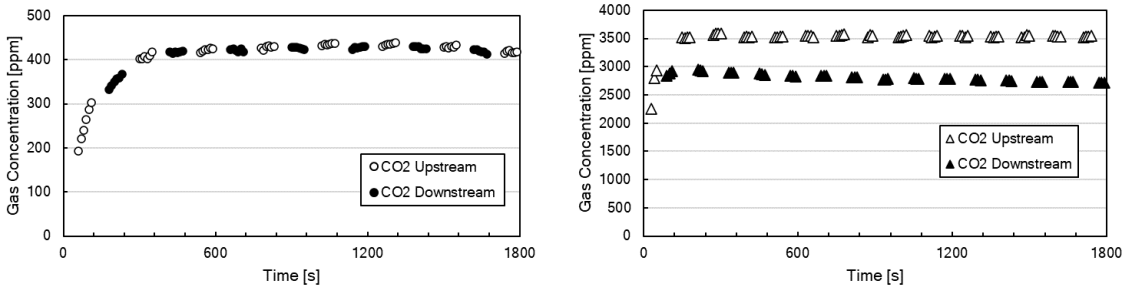


(a) (b)

Figure 43: Gas concentration versus time, $CO_2$, media A, (a) 60% R.H. (b) 5% R.H.

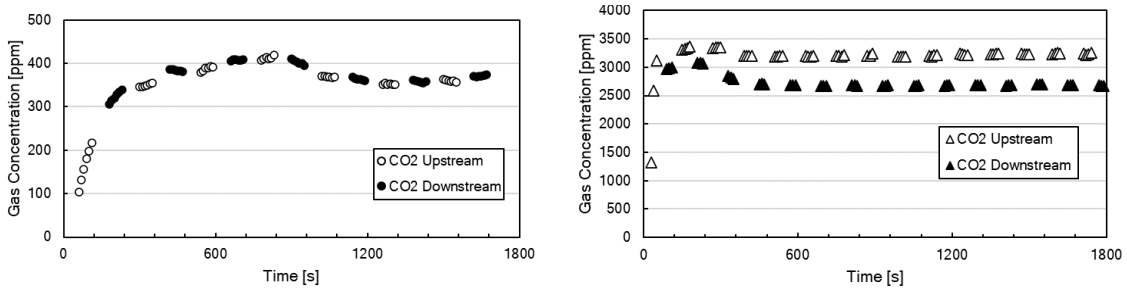


(a) (b)

Figure 44: Gas concentration versus time, $CO_2$, media B, (a) 60% R.H. (b) 5% R.H.

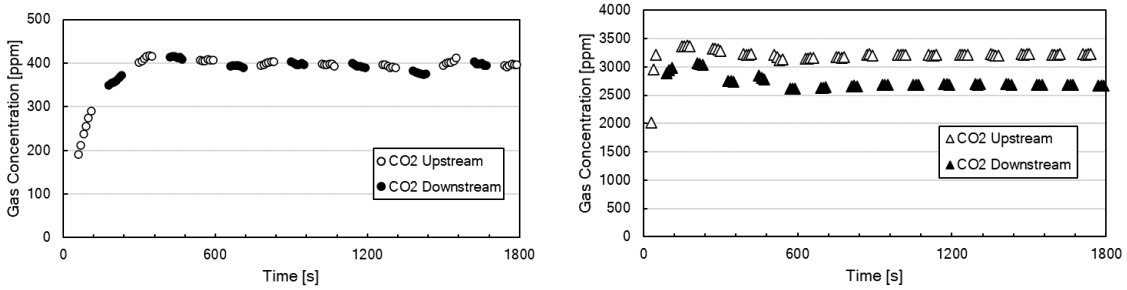


(a) (b)

Figure 45: Gas concentration versus time, $CO_2$, media C, (a) 60% R.H. (b) 5% R.H.

### 3.5.7 Discussion of Results

The first test parameter to examine was how well the indicated gas concentrations aligned with the target gas concentrations. To do this, the target gas concentration was first calculated using the known dilution ratio, recorded while operating the test bench, along with the known original span gas concentration. Next, the indicated gas concentration was calculated from the sensor outputs using the calibration factors obtained using the regression techniques described in section 3.4 and averaged during the 60-120s measurement period. The sample stream for gas concentration measurements was taken from the upstream, pre-filter sample port. The comparisons of mean indicated and target concentrations are listed below in table 13.

Table 13: Target and Mean Indicated Gas Concentrations

| Pollutant Gas | | Humid Condition | Dry Condition |
|---|---|---|---|
| NO | Target | 0.35 ppm | 0.25 ppm |
| | Indicated | 0.33 ppm | 0.24 ppm |
| CO | Target | 6.5 ppm | 20 ppm |
| | Indicated | 8.3 ppm | 21 ppm |
| $SO_2$ | Target | 1.5 ppm | 4.0 ppm |
| | Indicated | 2.7 ppm | 5.0 ppm |
| $CO_2$ | Target | 400 ppm | 3500 ppm |
| | Indicated | 410 ppm | 3350 ppm |
| $NO_2$ | Target | 350 ppb | X |
| | Indicated | 20→60 ppb | X |
| $NO_2 + O_3$ | Target | 350 ppb | X |
| | Indicated | 0→30 ppb | X |

The mean indicated gas concentrations were near expected for both humid and dry conditions for NO, CO, and $CO_2$. This was not true for testing of $SO_2$ and $NO_2$. Indicated values of $SO_2$ were 25 to 80% higher than the target, suggesting test system or calibration issues. On the other hand, indicated $NO_2$ concentrations were much lower, starting near zero and slowly increasing reaching final values at least 5 times lower than target values. Both the $NO_2$ and the combined $NO_2$ / $O_3$ sensors showed the same trends suggesting that this was not an individual sensor problem, and rather a system issue. Problems with the dilution air supply was the only explanation considered plausible.

The expected upstream $NO_2$ concentration for $NO_2$ media testing was 350 ppb. Observed concentrations were much lower than expected during testing and increased during the 30-minute test. The concentration is determined by concentration and flow of span gas and the flow of dilution air. The ratio of dilution airflow to span gas flow determines how much the span gas is diluted. The concentration of $NO_2$ in the span gas was 5ppm, the span gas flow was set to 2LPM, and the dilution airflow was set to 27LPM giving a dilution factor of 1:14.5, which should have led to a diluted gas concentration of 350ppb, so that is what was expected. The system for controlling the span gas flow could be very robust, but the system for controlling dilution airflow depends on a well-regulated supply of dry compressed air. If we assume that the compressor is operating near its capacity, the dilution air used during $NO_2$ testing could have reduced system air pressure and decreased flow over time. This could explain the increase in concentration during the course of the test but does not explain the very low concentrations, 5-10x lower than expected.

Calibration of the $NO_2$ sensors was not considered as a possible cause of the indicated low concentration because the calibration was performed on the same day and produced good results as described above. This suggests that calibration was not the cause of the drifting and low concentration results shown in figures 41 and 42 of section 3.5.5, rather, that values in 3.5.5 are the correct indicated concentrations from the $NO_2$ sensors, but the dilution system is not providing the expected concentration.

Another key objective of this study was to determine the effectiveness of each media in removing each pollutant gas. Due to the sensor noise limitations already described, many of the low removal efficiency media tests could not be analyzed accurately. Pollutant gas removal efficiency results are compiled in Table 14 below. Differences of less than 5% are approaching sensor noise and simply reported as less than 5% removal efficiency.

Table 14: Pollutant Gas Removal Efficiency of each Media

| **Pollutant Gas** | **Media** | **Humid Removal Efficiency [%]** | **Dry Removal Efficiency [%]** |
|---|---|---|---|
| NO | A | 11 | 39 |
| | B | 15 | 32 |
| | C | 6 | 11 |
| CO | A | <5 | <5 |
| | B | <5 | <5 |
| | C | <5 | <5 |
| $SO_2$ | A | 5 | 81 |
| | B | <5 | 72 |
| | C | <5 | X |
| $CO_2$ | A | <5 | 22 |
| | B | <5 | 17 |
| | C | <5 | 17 |
| $NO_2$ | A | <5 | X |
| | B | <5 | X |
| $NO_2 + O_3$ | A | <5 | X |
| | B | <5 | X |

From table 14 we see drastic influence of humidity on the gas removal effectiveness for each media and gas combination. For example, the removal efficiency of NO was greater than 30%, when dry, for media A and B, though this dropped to 15% or less when tested with higher humidity conditions. A likely explanation for this is that activated carbons have an affinity for water vapor, and this could limit the sorption capacity for the pollutant gases. This effect was exhibited by each of the media that had a distinguishable removal efficiency. Some conditions did not allow for distinguishable concentration differences between upstream and downstream samples. This was due to low gas removal effectiveness for some gas and media combinations. These results were considered as a less than 5% removal efficiency.

## *3.6 Chapter 3 Conclusions*

This study had aimed to evaluate pollutant gas removal effectiveness for a collection of carbon media, and to also evaluate a set of low-cost gas sensors (LCGS) for use in monitoring ambient-high levels of common indoor pollutant gases. This was guided by two objectives: 1) Determine the performance of the LCGS based on a set of defined metrics. 2) Measure the gas removal effectiveness under typical indoor conditions.

A purpose-built test bench was designed and built for the project. It was capable of flowing diluted pollutant gases through panel style carbon media at 5cm/s face velocity with automated sample line switching, humidity control, and data logging.

The first objective was accomplished by evaluating sensor accuracy, noise, and response time. With respect to sensor accuracy, it was found that mean indicated gas concentrations were near expected during testing conditions for NO, $NO_2$, $SO_2$, CO, and

$CO_2$. Media testing results for $SO_2$ an $NO_2$ were not as expected, though dilution air problems were the suspected cause for gas concentrations differing from the target value. Considering the accurate calibration on the sensors, it was likely that each of the sensors were still measuring accurately and indicating the true concentration. When evaluating sensor noise, it was found that NO, $NO_2$, $NO_2/O_3$, and $CO_2$ had observed noise that was lower than the manufacturer specifications. Noise was higher than the specification value for $SO_2$ and CO, where the $SO_2$ sensor exhibited 83ppb of noise compared to the spec of 5ppb and the CO sensor exhibited 31ppb of noise versus the manufacturer spec of 4ppb. In consideration of response times, the $CO_2$ and CO sensors were slower than manufacturer specification, the $NO_2$ and $NO_2/O_3$ nearly matched specification, and the NO and $SO_2$ sensors were faster than specification.

The second project objective was the evaluation of media gas removal efficiencies. Pollutant gas removal efficiency was determined using the indicated concentration measurements from each respective LCGS for each of the pollutant gas and carbon media combination tested under both dry and humid conditions. Removal efficiencies were very low for CO and $NO_2$. They were somewhat higher for NO, $SO_2$, and $CO_2$, most notably under dry conditions. This work demonstrated the efficacy of using LCGSs for media evaluation.

# Chapter 4: Recommended Further Work

## *4.1 Investigation of the Temperature Dependent Effects in Crankcase Aerosol Control Devices*

Additional experiments and modeling would be useful to further test the shrinkage and regrowth growth theory. They would also aid in better explaining oil property dependent effects, such as the greater shifts in MPPS with temperature for certain oils, as well as the apparent negative filtration efficiency exhibited by the coalescing filter when separating the high volatility oil mix.

Testing for this project was completed without dilution. This made vapor phase components available for condensation when the sample was cooled to ambient during transport in the sampling lines. Isothermal heated sampling lines are the first consideration, though they will not stop the constant evaporation of components not already entirely lost. Instead, sampling with dilution probes would allow for removal of most of the vapors and quench regrowth processes, making the particles measured more representative of the particles in the test bench that are entering and leaving the removal device.

Another useful test would be to test removal efficiency with dry coalescing media rather than a saturated coalescing filter. The performance of such media could be predicted more accurately by SFE theory and be used to better interpret saturated condition results.

Another valuable test would be operating these devices, both the coalescing filters and inertial separators, with solid particles. Solid particles would not be influenced by shrinkage and regrowth processes exhibited by the oil mist droplets.

The last consideration for further work would be advanced modeling of the evaporation and condensation for multi-component lubricating oil droplets. Recall that the model observed in this study was for homogenous droplets, thus heterogeneous intermolecular reactions were not accounted for. Advanced modeling of this sort would prove vital in the understanding of the particle mechanics observed as well as in many other fields where volatile multicomponent droplets in air are observed.

## *4.2 Evaluation of Media and Low-Cost Gas Sensors for Indoor Air Quality Measurement*

Further testing in the evaluation of media and LCGSs for indoor air quality measurement would primarily be focused on testing additional products, considering other environmental influences, long-term testing, and operating in tandem with high accuracy instruments.

First, additional testing for other LCGS products will need to be performed because new technologies are constantly being developed and released. The technology as a whole is currently an evolving field where production cost is a large drawback. Emerging technologies and product development methods for accomplishing low-cost gas sensing at further reduced cost will instigate integration with air control devices.

Other environmental influences to test the effects on media and LCGS would be temperature. For either the media or sensors to be used reliably in other markets globally, testing at air temperatures from 0 to 40°C should be performed.

The third consideration for additional testing would be to incorporate long-term experiments. Low-cost gas sensors have been known to lose calibration after months of use

and this may be dependent on exposure conditions. If a sensor integrated with an air quality control device loses calibration, the sensor(s) will have to be re-calibrated or replaced. In a marketing sense, the sensor suppliers are interested in producing a replaceable or serviceable product, as this is often where profits are encompassed. Though, a replaceable product also needs to have a balance between replacement cost and service interval, else consumers may be driven away.

The final recommendation for further work is to include high accuracy gas analyzers in the testing equipment. The analyzers could be operated in parallel with a LCGS package to acquire accurate concentration measurements and they could also be used to better calibrate the LCGSs.

# References


[1] J. Heywood, *Internal Combustion Engine Fundamentals*. McGraw-Hill Education, 1988.

[2] A. Irimescu, S. di Iorio, S. S. Merola, P. Sementa, and B. M. Vaglieco, "Evaluation of compression ratio and blow-by rates for spark ignition engines based on in-cylinder pressure trace analysis," *Energy Convers Manag*, vol. 162, pp. 98–108, Apr. 2018, doi: 10.1016/j.enconman.2018.02.014.

[3] D. Uy *et al.*, "Correlating Laboratory Oil Aerosol Coking Rig Tests to Diesel Engine Tests to Understand the Mechanisms Responsible for Turbocharger Compressor Coking," in *SAE Technical Papers*, Mar. 2017, vol. 2017-March, no. March. doi: 10.4271/2017-01-0887.

[4] M. L. Lorenz, T. Koch, G. Kasper, J. Pfeil, and N. Nowak, "Origin and Separation of Submicron Oil Aerosol Particles in the Blow-by of a Heavy-Duty Diesel Engine," *International Journal of Engines*, vol. 13, no. 3, pp. 363–376, 2020, doi: 10.2307/27034060.

[5] B. A. Pardue, "Fundamentals of Crankcase Ventilation Open and Closed Systems," 2004.

[6] E. Tatli and N. N. Clark, "Crankcase Particulate Emissions from Diesel Engines," *International Journal of Fuels and Lubricants*, vol. 1, no. 1, pp. 1334–1344, 2009, doi: 10.2307/26272097.

[7] EPA, "Proposed Rules: Control of Air Pollution From New Motor Vehicles: Heavy-Duty Engine and Vehicle Standards ," Vol. 87, No. 59 , Mar. 2022.

[8] N. Nowak *et al.*, "On aerosol formation by condensation of oil vapor in the crankcase of combustion engines," *Aerosol Science and Technology*, vol. 56, no. 2, pp. 101–116, 2021, doi: 10.1080/02786826.2021.1976720.

[9] V. Golkarfard, R. Subramaniam, J. Broughton, A. King, and A. Mullins, "Comparative Performance of 12 Crankcase Oil Mist Separators," pp. 5–14, 2019.

[10] W. Krause, K. H. Spies, L. E. Bell, and F. Ebert, "Oil Separation in Crankcase Ventilation - New Concepts Through System Analysis and Measurements," *Journal of Engines*, vol. 104, 1995.

[11] T. A. Dollmeyer *et al.*, "Meeting the US 2007 Heavy-Duty Diesel Emission Standards-Designing for the Customer."

[12] W. C. Hinds, *Aerosol Technology*, 2nd ed. New York: John Wiley and Sons, 1999.

[13] R. Mead-Hunter, A. J.C. King, and B. J. Mullins, "Aerosol-mist coalescing filters - A review," *Sep Purif Technol*, 2014.

[14] Center for Filtration Research, "Filter Modeling & Design Tool," *https://cfr.umn.edu/*, 2021.

[15] “ISO 17536-4: Road Vehicles - Aerosol separator performance test for internal combustion engines - Part 4: Laboratory fractional efficiency test method,” 2019.

[16] B. Y. H. Liu, D. Y. H. Pul, K. L. Rubow, and W. W. Szymanski, “Electrostatic Effects in Aerosol Sampling and Filtration,” 1985. [Online]. Available: https://academic.oup.com/annweh/article/29/2/251/167459

[17] Dekati Ltd., “ELPI User Manual,” 2008.

[18] Z. Liang *et al.*, “Comprehensive chemical characterization of lubricating oils used in modern vehicular engines utilizing GC × GC-TOFMS,” *Fuel*, vol. 220, pp. 792–799, May 2018, doi: 10.1016/j.fuel.2017.11.142.

[19] A. Razzouk, R. A. Naccoul, I. Mokbel, J. Saab, and J. Josef, “Vapor and sublimation pressures of three normal alkanes: C20, C24, and C28,” *J Chem Eng Data*, vol. 54, no. 4, pp. 1214–1219, Apr. 2009, doi: 10.1021/je800534x.

[20] R. W. Elliott and H. Watts, “Diffusion of some Hydrocarbons in Air: a Regularity in the Diffusion Coefficients of a Homologous Series,” 1971.

[21] P. C. Raynor and D. Leith, “The Influence of Accumulated Liquid on Fibrous Filter Performance,” *J Aerosol Sci*, vol. 31, no. 1, pp. 19–34, Jan. 2000, doi: 10.1016/S0021-8502(99)00029-4.

[22] S. Abishek, R. Mead-Hunter, A. J. C. King, and B. J. Mullins, “Capture and re-entrainment of microdroplets on fibers,” *Phys Rev E*, vol. 100, no. 4, p. 042803, Oct. 2019, doi: 10.1103/PhysRevE.100.042803.

[23] United States Environmental Protection Agency, “Indoor Air and Coronavirus (COVID-19),” *https://www.epa.gov/coronavirus/indoor-air-and-coronavirus-covid-19*, 2022.

[24] Grand View Research, “Air Purifier Market Size, Share & Trends Analysis Report By Technology (HEPA, Activated Carbon, Ionic Filters), By Application (Commercial, Residential, Industrial), By Region, And Segment Forecasts, 2022 - 2030,” 2021.

[25] S. Sircar, T. C. Golden, and M. B. Rao, “Activated Carbon for Gas Separation and Storage,” 1996.

[26] “A Tribute to Robert Mitchell Milton, Zeolite Pioneer (1920-2000),” *Microporous and Mesoporous Materials*, vol. 47, no. 1, pp. 119–126, Sep. 2001, doi: 10.1016/S1387-1811(01)00301-8.

[27] E. M. Flanigen, “Molecular sieve zeolite technology - the first twenty-five years,” *Pure and Applied Chemistry*, vol. 52, no. 9, pp. 2191–2211, Jan. 1980, doi: 10.1351/pac198052092191.

[28] R. M. Milton, “Molecular Sieve Adsorbents,” 1959

[29] J. M. Dias, M. C. M. Alvim-Ferraz, M. F. Almeida, J. Rivera-Utrilla, and M. Sánchez-Polo, “Waste materials for activated carbon preparation and its use in

aqueous-phase treatment: A review," *Journal of Environmental Management*, vol. 85, no. 4. pp. 833–846, Dec. 2007. doi: 10.1016/j.jenvman.2007.07.031.

[30] O. Ioannidou and A. Zabaniotou, "Agricultural residues as precursors for activated carbon production-A review," *Renewable and Sustainable Energy Reviews*, vol. 11, no. 9. pp. 1966–2005, Dec. 2007. doi: 10.1016/j.rser.2006.03.013.

[31] N. Sánchez-Bastardo, R. Schlögl, and H. Ruland, "Methane Pyrolysis for Zero-Emission Hydrogen Production: A Potential Bridge Technology from Fossil Fuels to a Renewable and Sustainable Hydrogen Economy," *Ind Eng Chem Res*, vol. 60, no. 32, pp. 11855–11881, Aug. 2021, doi: 10.1021/acs.iecr.1c01679.

[32] W. Yao, D. L. Gallagher, and A. M. Dietrich, "An overlooked route of inhalation exposure to tap water constituents for children and adults: Aerosolized aqueous minerals from ultrasonic humidifiers," *Water Res X*, vol. 9, p. 100060, Dec. 2020, doi: 10.1016/j.wroa.2020.100060.

[33] Sensor Technology House, "How Electrochemical Gas Sensors Work - Alphasense Application Note 104," 2013.

[34] Sensor Technology House, "NO-B4 Nitric Oxide Sensor - Technical Specification," 2019.

[35] Sensor Technology House, "CO-B4 Carbon Monoxide Sensor - Technical Specification ," *https://www.alphasense.com/wp-content/uploads/2022/09/Alphasense_CO-B4_datasheet.pdf*, 2022.

[36] Sensor Technology House, "SO2-B4 Sulfur Dioxide Sensor - Technical Specification," *https://www.alphasense.com/wp-content/uploads/2019/09/SO2-B4.pdf*, 2019.

[37] Sensor Technology House, "NO2-B43F Nitrogen Dioxide Sensor - Technical Specification," *https://www.alphasense.com/wp-content/uploads/2022/09/Alphasense_NO2-B43F_datasheet.pdf*, 2022.

[38] Sensor Technology House, "IRC-A1 Carbon Dioxide Infrared Sensor - Technical Specification," *https://www.alphasense.com/wp-content/uploads/2018/04/IRC-A1.pdf*, 2018.

# Appendix 1: Leak Testing Benchtop Flow Apparatuses

The test benches in Chapter 2 and Chapter 3 were leak tested using a TSI ultrafine condensation particle counter (CPC) 3776 and a sanitary fitting pipe with sampling probe. The sanitary fitting pipe was interchangeable with each of the apparatus piping components. Starting from the HEPA filter inlet of each system, the sampling probe pipe was swapped for each piping component one-by-one and connected to a CPC to detect particle leakage upstream. As the upstream components were confirmed to have no leakage, the sampling pipe continued to be swapped for further downstream components and tested for upstream system leakage until the sampling pipe was the last component to the system. Leakage rates were controlled to a particle count of zero as measured by the ultrafine CPC. The average particle concentration for the ambient lab environment was 7000#/$cm^3$.

# Appendix 2: Instrument Schematics

Dekati Electrical Low-Pressure Impactor

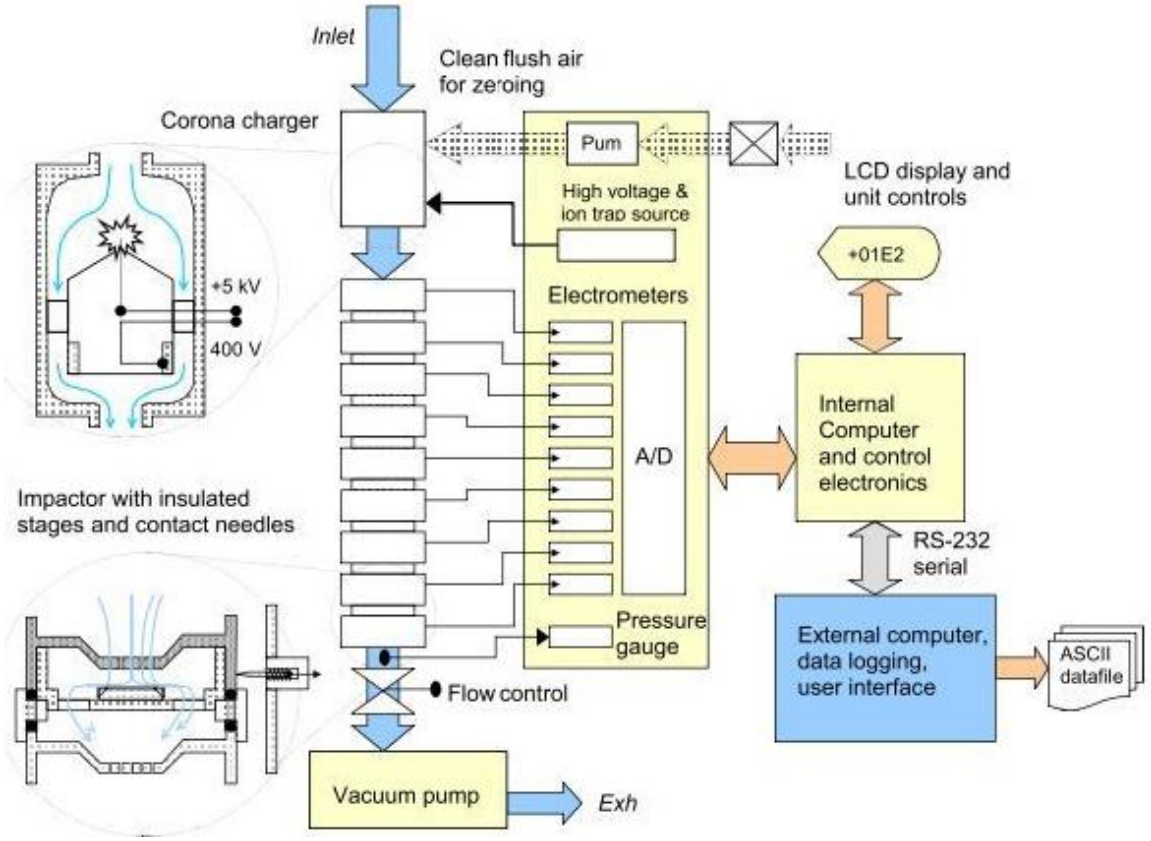


Figure A.2.1:Operation and internals diagram of Dekati ELPI[17]

The Dekati ELPI is an impactor type particle size spectrometer used for real-time particle size distribution measurements. The ELPI was used for each of the projects in Chapters 2 and 3. The instrument was operated at 10[L/min] of nominal flow, measuring with the largest current range possible of 400,000[fA]. The D50 cutoff sizes for the impaction plates, in microns, of the 13 stages from largest to smallest are: 8.0953, 5.1766, 3.2085, 2.0422, 1.2999, 0.8178, 0.5163, 0.3296, 0.2149, 0.1373, 0.0829, and 0.0435. Note these are aerodynamic diameters.

# Appendix 3: Particle Removal Efficiency Testing the Carbon Panel Media

Particle removal testing was not a focus of the study presented in Chapter 3, though it was a supplementary consideration and was possible to incorporate without major deviation. The test apparatus presented in 3.3 was adequate for flowing and testing with solid particles, the only changes were installing isokinetic sampling tips to the sample ports and an inlet section of the bench being exchanged for a t-fitting to connect to the atomizer.

Tap water was used at the base liquid used in the nebulizer type aerosol generator. The atomizer system was equipped with desiccant dryers to remove water vapor, and a Kr-85 neutralizer to produce an equilibrium charge distribution. The output of the tap water generated aerosol is well understood to be composed of calcium and magnesium ions [32].

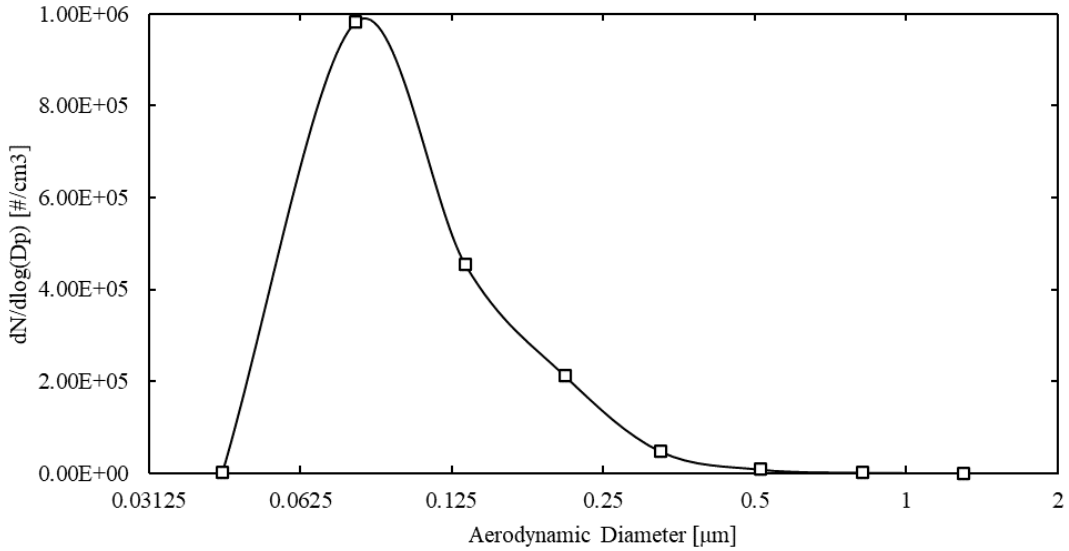


Figure A.3.1: Normalized number distribution of test aerosol produced with atomized tap water

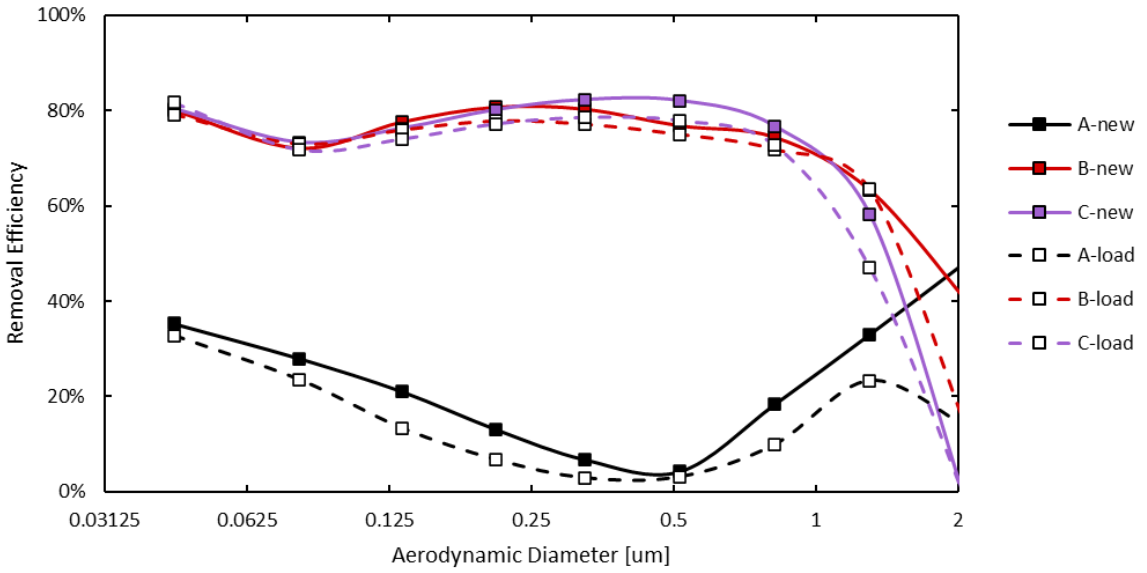


Figure A.3.2: Removal efficiency for media A, B, C. New and load conditions shown.

In Figure A.3.2, data is presented for the 3 carbon media types with two initial load conditions. A single piece of media being tested was analyzed for two conditions denoted as “new” and “load”. The new test condition was measured between minutes 3 and 5 of loading, and the load test condition was measured after 30 minutes elapsed.